A Final Report for

A Massively Parallel Particle Code for Rarefied Ionized and Neutral Gas Flows in earth and Planetary Atmospheres, Ionospheres and Magnetospheres

NASA Grant NAG5-9464 from the Applied Information Systems Research Program

for the period April 15, 2000 to April 14, 2004

Principal Investigator

Michael R. Combi
Department of Atmospheric, Oceanic and Space Sciences
University of Michigan
Space Research Building
2455 Hayward Street
Ann Arbor, MI 48109
Tel: 1 (734) 764-7226
Fax: 1 (734) 647-3083
Email: mcombi@umich.edu

I. Introduction

In order to understand the global structure, dynamics, and physical and chemical processes occurring in the upper atmospheres, exospheres, and ionospheres of the Earth, the other planets, comets and planetary satellites and their interactions with their outer particles and fields environs, it is often necessary to address the fundamentally non-equilibrium aspects of the physical environment. These are regions where complex chemistry, energetics, and electromagnetic field influences are important. Traditional approaches are based largely on hydrodynamic or magnetohydrodynamic (MHD) formulations and are very important and highly useful. However, these methods often have limitations in rarefied physical regimes where the molecular collision rates and ion gyrofrequencies are small and where interactions with ionospheres and upper neutral atmospheres are important.

At the University of Michigan we have an established base of experience and expertise in numerical simulations based on particle codes which address these physical regimes. The Principal Investigator, Dr. Michael Combi, has over 25 years of experience in the development of particle-kinetic and hybrid kinetic/hydrodynamics models and their direct use in data analysis as well as for theoretical studies. He has also directed and performed ground-based and space-based remote observational work and participated on spacecraft instrument teams. His research has involved studies of cometary atmospheres and ionospheres and their interaction with the solar wind, the neutral gas clouds escaping from Jupiter's moon Io, the interaction of the atmospheres/ionospheres of Io and Europa with Jupiter's corotating magnetosphere, as well as Earth's ionosphere.

Support from NASA's Applied Information Systems Research Program (AISRP) has resulted in the construction and first applications of three-dimensional, neutral and ion kinetic particle models, which have application to various space science problems.

II. Progress and Current Status of the Kinetic Modeling Program

As part of our AISRP project we have developed massively parallel code for performing kinetic calculations for neutral and ionized gases in space science applications. First we will describe some general work on the computational mesh. Then we will briefly describe an application to the plasma interaction of Jupiter's magnetized plasma torus with the satellite Io, and show some exciting new results. Thirdly, we will describe in more detail an application to the expanding neutral atmosphere of a comet.

An Unstructured Computational Mesh

The original plan at the beginning of our AISRP grant was to adopt the hierarchical Cartesian mesh algorithm used by our colleagues at the University of Michigan, lead by Dr. Tamas Gombosi. It became clear, in using and testing our own code, that the overhead in memory required for implementing their block-based parallel scheme, which works well for them in MHD, is far too inefficient in general for the more memory-intensive particle kinetic methods. At the same time, Dr. Gombosi's group itself has been in the process of interfacing their code with modules from other groups, by simply translating results between models where the spatial mesh of each model is optimized to the model in question. It was clear we should adopt the best computational mesh for our own problems.

We spent considerable time developing an unstructured mesh, which is far more efficient for particle-based algorithms like ours. It is based on triangles for two-dimensional problems and tetrahedrons in three dimensions. This approach provides great flexibility in being able to conform to planetary-type problems where there is a spherical inner body or an irregular comet as well as to very extended spatial regimes where a wide range of computational cell sizes is required. For example in Figure 1 we show a comparison of an old (*Combi* 1996) geometrical-based structured radial-polar 2D-axisymmetric mesh used for an expanding cometary atmosphere with an unstructured triangular mesh. Because of the efficiency gained in parallelization and the large memory of modern computers, we now use far more computational cells than the PI used 8 years ago.

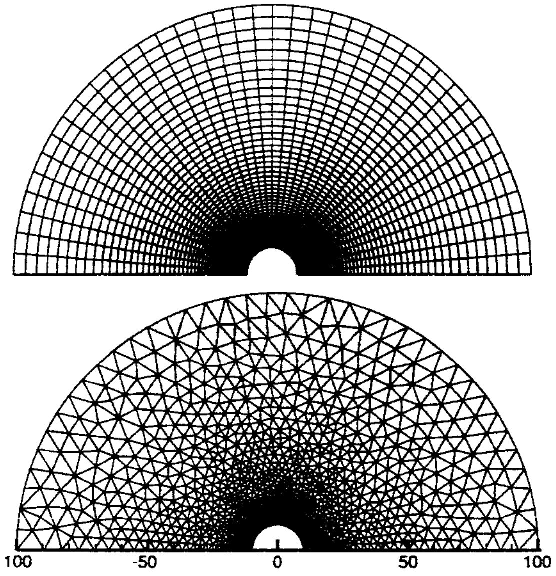

Figure 1. Comparison of a Structured and Unstructured Computational Mesh.

The flexibility and power of this approach will be more apparent when we first apply it to a non-spherical central body, Comet Borrelly. See Figure 2. The triangles on the surface serve as the faces of the tetrahedrons at the boundary of the kinetic calculation. Science applications such as this, which are supported by NASA missions and science-topic specific Research and Analysis grants, illustrate the synergistic importance of the AISRP support for basic development of computer methodologies and algorithms.

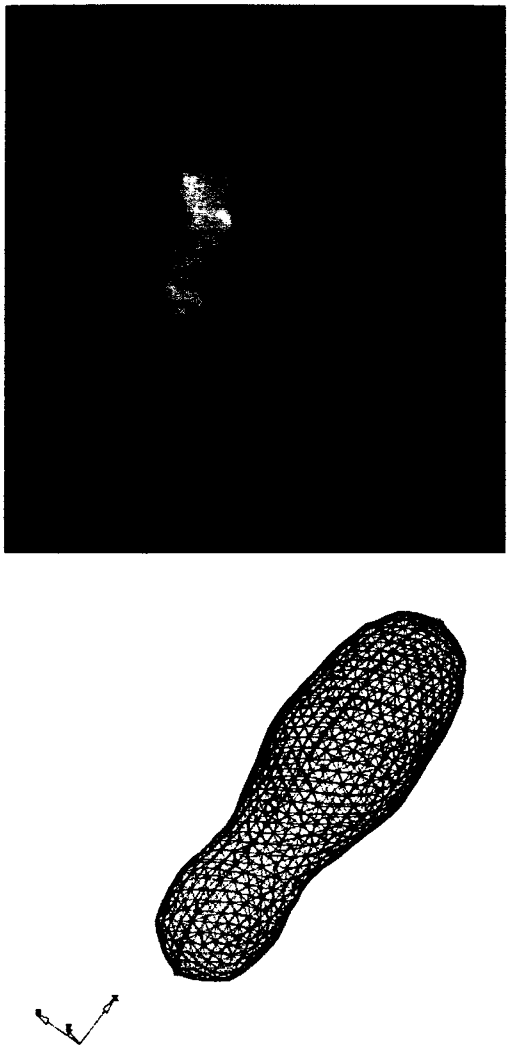

Figure 2. Image of Comet Borrelly from Deep Space 1. Below is the 3D mesh for an axisymmetric approximation to the shape of comet Borrelly.

A Kinetic Simulation for the Interaction of Jupiter's Plasma Torus with Io

For plasma particle simulations, we have been studying the interaction of Jupiter's plasma torus with the volcanic satellite Io. The kinetic particle method allows us to treat the important non-equilibrium aspects of the physics that are important in the near Io environment. From our first results it appears that the major effect is from the ring-beam shape of the velocity distribution function for pickup ions near Io. Our best MHD simulation (*Combi et al.* 2002) of the interaction compared with Galileo data is shown in Figure 3 and results from assuming that the ratio of the specific heats, ρ, is 2 instead of 5/3. This at least accounts for fact that a gyration-dominated plasma should act as if there are only 2 kinetic degrees of freedom.

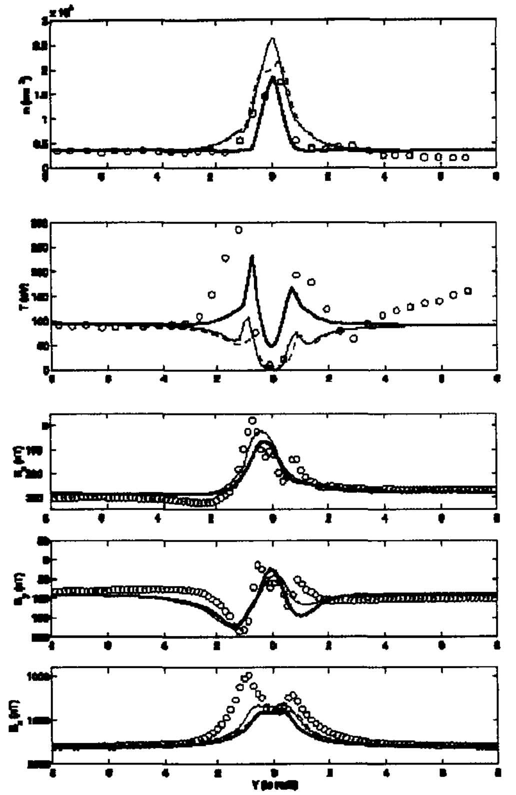

Figure 3. MHD Model Results Compared with Galileo Measurements. From the top, down are plasma density, temperature and three components of magnetic field.

In particle simulations the explicit modeling of the ion gyrations means that we can maintain ring-beam distribution of pickup ions along with their diamagnetic effect. Figure 4 shows the distribution of density, temperature and the N/S component of the magnetic field (Lipatov and Combi, 2004). We see that the diamagnetic effect of the pickup ions increases the temperature in the flanks of the wake (the two temperature peaks) and broadens the magnetic field perturbation, markedly improving even the best MHD result. Such anisotropic pressure effects are mediated by wave-particle scattering and collisional scattering with the neutral exosphere, which are modeled consistently and naturally in the kinetic simulation.

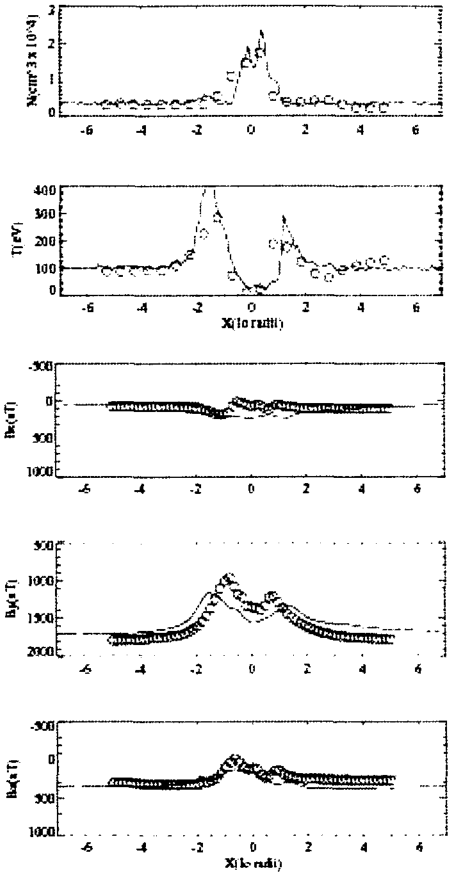

Figure 4. Results of Particle Kinetic Model for the Galileo J0 Flyby. From the top down are results of number density, temperature and the N/S component of the B field. The non-isotropic pressure effects of the gyration dominated pickup ions produce the temperature peaks and broad B field perturbation.

A Kinetic Simulation for a Gaseous Coma

The cometary atmosphere is a unique phenomenon in the solar system. Owing to its negligible gravity, comets produce a highly variable and extensive atmosphere with a size much larger than the characteristic size of the cometary nucleus. As the comet approaches the sun, water vapor with other gases sublimates, generating an escaping atmosphere from the surface of nucleus, which consists of ice and refractory materials (rocky and organic solids and dust). Sublimating gas molecules undergo frequent collisions and photochemical processes in the near nucleus region. Except in the case of bright comets like Halley, Hyakutake, and Hale-Bopp on their close approaches to the sun, much of the time and for most of the coma, the gas production rate is small enough that the gas flow is in a high Knudsen number regime except for the immediate regions around active areas on the sunlit nucleus. [The Knudsen number is defined as the ratio between the collisional mean free path between molecules and the local length scale of interest in the problem.] This is especially true for the short period comets which are on the target lists for recent and upcoming NASA and NASA-participating ESA missions to comets.

Two-dimensional axisymmetric models for six species (H_2O, CO, OH, H_2, O, H) have been performed using our new parallelized code. A hard sphere collision model was assumed for intermolecular collisions. For water-water collisions the viscosity equivalent cross section (*Crifo* 1989) has been used. For other collision pairs, collision cross sections based on relevant atomic data (*Combi* 1996) were used.

We performed calculations based on conditions expected for the then target of the upcoming Rosetta mission to comet Wirtanen (*Tenishev and Combi,* 2002). The rescheduling to the sucessful launch this year to Comet 67P/Churyumov-Gerasimenko means it will have somewhat different specific characteristics, but the breakdown of simple pure fluid conditions will be otherwise similar to these results.

The nucleus of Wirtanen was assumed to be spherical with a radius of 0.6 km and have axisymmetric gas emission. The gas flux from the dayside is controlled by absorption of solar radiation, and the flux varies as the square of the cosine of the subsolar angle. It was assumed that only two gaseous species sublimate from the surface: H_2O and CO. Both species are in equilibrium with the surface, and the outflow mixture is partitioned with 80% for H_2O and 20% for CO. As representative cases we performed calculations for the comet at its most active at perihelion of 1.05 AU ($Q = 5 \times 10^{27}$/s) as well as farther away at 1.5 AU ($Q = 8 \times 10^{26}$/s). For the nominal mission the comet spends most of the mission time at distances larger than 1.5 AU, and as we find, the collisional regime is already rarefied enough so that a particle approach is already needed. The larger and smaller production rate conditions are actually relevant for the new Rosetta target comet Churyumov-Gerasimenko at its perihelion distance of 1.5 AU and at 2.0 AU, respectively.

In our paper (*Tenishev and Combi,* 2002) we describe in detail the comparison of the flow fields and collisional regimes for the two cases. The salient aspects can be told using only the Knudsen number plot for the 1.5 AU case as well as the radial velocity fields at both cases. These are shown in Figures 5 a, b, and c. What we find is that for the comet at 1.5 AU, only the region near the nucleus and immediately above the active area is in a low Knudsen number (collisional fluid) regime. For the case at 1.05 AU (perihelion) the entire region near the nucleus is in a low Knudsen number regime and the flow conditions can be understood in terms of a hydrodynamic calculation. The effects of the two different collisional regimes are illustrated by the different radial velocity fields (Fig. 4 b and c).

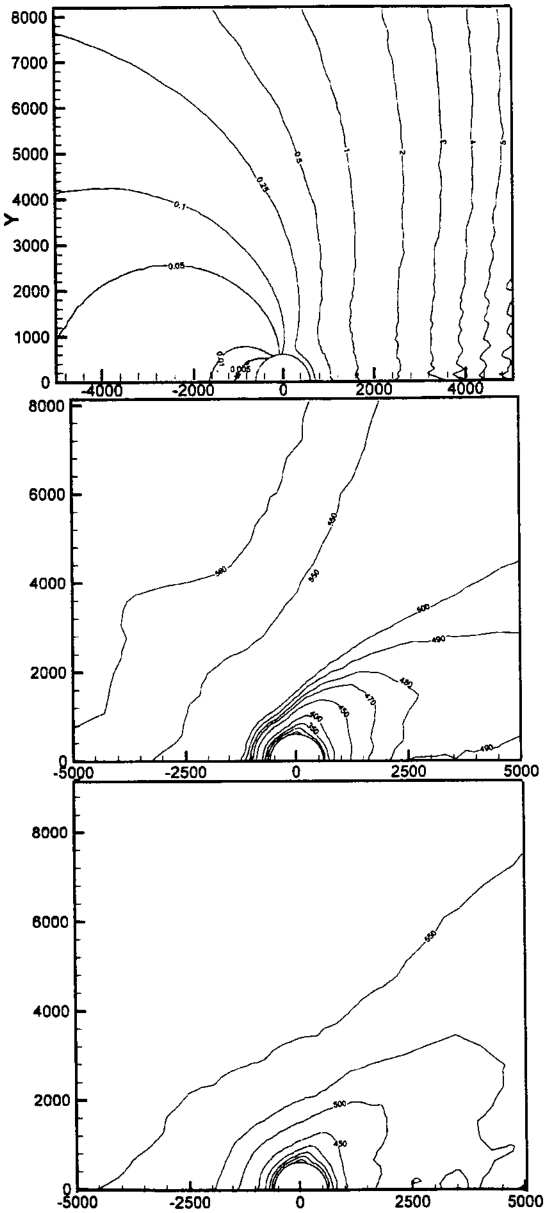

Figure 5. DSMC Results for Comet Wirtanen. The top plot shows the Knudsen number for the model at 1.5 AU where the shaded region is in the low Knudsen number (<0.1) state. The middle and bottom plots are contours of radial velocity for 1.5 and 1.05 AU, respectively. The differences are due to the rarefied density for the 1.5 AU conditions.

In the more rarefied case the adiabatic acceleration of the flow proceeds more slowly. The situation would be even worse for the comet at much larger heliocentric distances, where most of the Rosetta mission actually takes place.

Dusty-Gas Hydrodynamics and Kinetics

We already have incorporated multiple dust particle-size populations in the DSMC code. This has direct applications for the dusty-gas comae of comets and volcanic plumes on planetary satellites such as Jupiter's Io and Neptune's Triton. The dust particles can fragment and sublimate to serve as an extended source of gas. We have completed the testing of the dusty-gas kinetic calculation in the fluid limit, and it does reproduce published dusty-gas hydrodynamics calculations of *Gombosi et al.* (1986). The description of the Euler equations for a dust-gas cometary coma have been described in detail in many papers, including some by our own group at the University of Michigan (*Combi et al.* 1999, *Körösmezey and Gombosi* 1989). One can write down equation of conservation of mass, momentum and energy for the gas

$$\frac{\delta\delta}{\delta t} + \delta\ \delta(\delta \mathbf{u}) = \frac{\delta\delta}{\delta t},$$

$$-\frac{-\mathbf{u}}{-t} + -(\mathbf{u} -)\mathbf{u} + -p = -\mathbf{F},$$

$$\frac{1}{\nabla\nabla 1}\frac{\nabla p}{\nabla t} + \frac{1}{\nabla\nabla 1}(\mathbf{u}\,\nabla\nabla)p + \frac{\nabla}{\nabla\nabla 1}p(\nabla\,\nabla\mathbf{u}) = \nabla Q_{gd} + Q_{ph}\,\nabla Q_{IR}$$

respectively, and for any number of dust particle-size populations

$$\frac{\delta\delta_i}{\delta t} + \delta\ \delta(\delta_i \mathbf{u}_i) = \frac{\delta\delta_i}{\delta t} \qquad i = 1,\ldots,N,$$

$$\nabla_i \frac{\nabla \mathbf{v}_i}{\nabla t} + \nabla_i(\mathbf{v}_i\,\nabla\nabla)\mathbf{v}_i = \mathbf{F}_i \quad i = \ldots,N$$

respectively, where ρ is the gas mass density, $\boldsymbol{u}$ is the gas velocity, p is the gas pressure, $\boldsymbol{v}_i$ and ρ_i are the velocity and mass density for dust particles of radius a_i. The term $\frac{\rho\rho}{\rho t}$ is the gas production source rate, and $\frac{\rho\rho_i}{\rho t}$ is the dust production source rate for particles of radius, a_i. **F** is the gas-dust drag force, which is related to the forces on the individual particle size populations as $\mathbf{F} = \sum\sum_{i\Sigma}^{N} \mathbf{F}_i$, where the size dependent force is given by $\mathbf{F}_i = \frac{3\rho_i}{4a_i\rho_{bi}} pC_D' \mathbf{s}_i$, where $\mathbf{s}_i = \frac{\mathbf{u}-\mathbf{v}}{\sqrt{2kT/m}}$, k is the Boltzmann constant, T is the gas temperature and m is the gas mean molecular mass. The accommodation of gas via collisions with hotter dust yields the dust-gas heat exchange rate Q_{gd} which is given as

$$Q_{gd} = \frac{\Sigma + 1}{\Sigma} \Sigma C_p u \sum_{i=1}^{N} (T_i^{rec} \Sigma T_i) St_i'$$

Here C_p is the gas heat capacity at constant pressure and the rest of the coefficients can be defined under the assumption of diffusive reflection such that:

$$C'_D = \frac{2\sqrt{-}}{3}\sqrt{\frac{T_i}{T}} + \frac{2s_i^2+1}{s_i^2\sqrt{-}}e^{-s_i^2} + \frac{4s_i^4+4s_i^2-1}{2s_i^3}erf(s_i)$$

$$T_i^{rec} = \left|1 + \frac{/\,|\,1}{/+1}s_i^2R_i'\right|T$$

$$R_i' = \frac{\frac{\pi}{\pi}2s_i + \frac{1\,\pi e^{\pi s_i^2}}{\pi\; s_i\pi\sqrt{\pi}} + \frac{\pi}{\pi}2s_i^2 + 2\pi\frac{1}{s_i^2}\frac{\pi}{\pi}erf(s_i)}{s_i\frac{e^{\pi s_i^2}}{\sqrt{\pi}} + \frac{\pi}{\pi}s_i^2 + \frac{1\pi}{2\pi}erf(s_i)}$$

$$St_i' = \frac{e^{|s_i^2}}{8s_i\sqrt{/}} + \frac{1}{8}\left|1 + \frac{1}{2s_i^2}\right|erf(s_i)$$

Finally, ρ_d is the bulk mass density of dust particles of radius a_i; T is the gas temperature, T_i is the dust temperature assumed in equilibrium with solar radiation. Otherwise the other intermediate quantities are s_i, the relative Mach number between gas and dust, C_D', the dust-gas drag coefficient, T_i^{rec}, the recovery temperature, R_i', the heat transfer function and St_i'. the Stanton number. Most of the dust-gas drag physics comes from the formulation by *Finson and Probstein* (1968) with later corrections discussed by *Wallis* (1982) and *Kitamura* (1986).

We have already used the dusty-gas kinetic model for modeling the dusty gas flow relevant for the NASA Deep Space 1 mission flyby of comet 21P/Borrelly (*Tenishev and Combi*, 2003). Results for the dust particle terminal velocities (i.e., the asymptotic velocities at large distances) as well as the acceleration profiles for different particle sizes are shown in Figure 6.

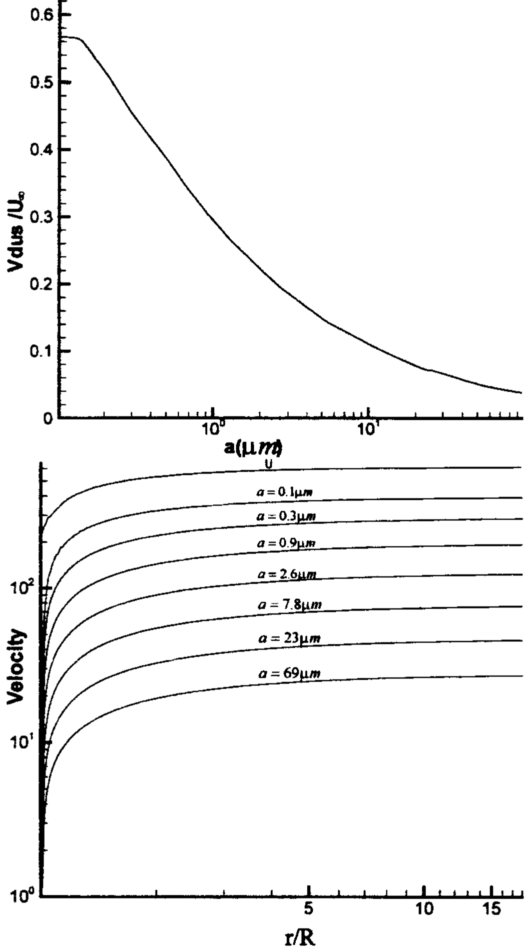

Figure 6. Results of Dusty-Gas Kinetic Calculations for Comet Borrelly during the Deep Space 1 Flyby. The upper plot shows the terminal velocity of dust particles as a function of dust particle sizes. The lower plot shows the velocities as a function of distance from the center of the nucleus.

III. Application of Developed Kinetic Modeling Tools for the NASA

Clearly the model codes and algorithms developed here will serve as the core of our own theoretical modeling and data anaysis tools for now and future. The models are being used as part of the PI's ongoing NASA programs: (1) NAG5-12822 Studies ofTenuous Planetary Atmospheres, (2) NAG5- 13239 Distribution of Gas in the Inner Comae of Comets. These projects will continue to support science applications and publications of the code and algorithms developed. These were also used as the basis for 3 proposals written in 2004 and submitted to planetary R&A programs to the 2004 ROSS NRA to study Jupiter's icy satellites and Mars' tenuous upper atmosphere, as well as for further proposed model and algorithm development under the AISRP. Model development and application is a sophisticated interdisciplinary and labor intensive effort, which is very difficult to support as minor parts of several focused space application oriented research grants. For the theoretical modeling community AISRP can provide something analogous to the Instrument Development programs (e.g., PIDDP), which are recognized by NASA as necessary to promote future basic development of instrumentation.

Finally, one of the important goals of the AISRP is to provide new computational tools for use in future NASA programs. An interdisciplinary international modeling effort was begun this year, organized by the International Space Science Institute (ISSI) in Bern, Switzerland, in association with the Rosetta project (ESTEC) and the JPL Rosetta project (the support and organizing infrastructure for US investigators on the Rosetta project). As part of this effort, this PI is the lead investigator in the area of dusty-gas coma modeling (with T. Gombosi, U. Michigan and N. Thomas, U. Bern). The larger effort involves several other teams of investigators performing (1) MHD modeling of the comet/solar-wind interaction (T. Gombosi, K. Hansen, and M. Combi, U Michigan), (2) nucleus and surface-boundary modeling (B. Davidsson, ESTEC and H. Rickman), (3) electron energetics (T. Cravens U. Kansas), (4) plasma hybrid modeling (U. Motschmann and T. Bagdonat, MPI Braunschweig), (5) coma chemistry (K. Altwegg, U. Bern, and the entire U. Michigan group). Rosetta Project Scientist G. Schwehm and US Rosetta Project (JPL) Scientist C. Alexander are also participants as are a number of other Rosetta scientists. The dusty-gas DSMC model will be an integral part of this modeling effort for the next 12 years or more. We have already begun a process which will lead to a set of coupled 3D models for the target comet in about a year, from the nucleus and out past the bow shock, including: nucleus porous upper surface layers, surface/coma Knudsen layer, dusty-gas coma, MHD and hybrid kinetic descriptions of the plasma interaction, coma chemistry, and electron energetics.

Publications/presentations under AISRP

Axisymmetric Dusty Gas-Kinetic Models for Comet 46P/Wirtanen. M.R. Combi, T.-M. Ho, and N. Thomas. *American Astronomical Society, DPS meeting #33, #20.18*, 2001.

DSMC Simulation of the Cometary Coma. V.M. Tenishev and M.R. Combi. *Proceedings of the International Symposium on Rarefied Gas Dynamics*, Whistler, BC, July 20 - 25, 2002.

DSMC Simulation of the Cometary Coma. M.R. Combi. and V.M. Tenishev *Asteroids, Comets, Meteors*, ESA Publications, Noordwijk, The Netherlands, 2002.

3D Boltzmann Simulation of the Io's Plasma Environment with Adaptive Mesh and Particle Refinement. A. S. Lipatov and M.R. Combi. *Eos Trans. AGU, 83*(47), *Fall Meeting Suppl. Abstract #SM21A-0529*, 2002.

Development of a General Purpose 3D DSMC Flow Solver on Unstructured Meshes. V. Tenishev and M.R. Combi. AIAA Paper 2003-3776, 2003.

Numerical Study of Dust and Gas Distributions in the Inner Coma of Comet Borrelly. V.S. Tenishev and M.R. Combi,. *American Astronomical Society, DPS meeting #35, #38.01*, 2003.

3D Boltzmann Simulation of Io's Plasma Environment: Comparison with Observational Data. A. S. Lipatov and M.R. Combi. *Eos Trans. AGU, 84*(47), *Fall Meeting Suppl. Abstract #P32A-1064*, 2003.

3D Hybrid Simulation of the Cometary Plasma Environment with Adaptive Mesh and Particle Refinement. A. S. Lipatov and M.R. Combi. *Eos Trans. AGU, 84*(47), *Fall Meeting Suppl. Abstract #SM31C-1121*, 2003.

DSMC Simulation of the Cometary Coma. V.M. Tenishev and M.R. Combi. *Rarefied Gas Dynamics: 23rd International Symposium. AIP Conference Proceedings, 663, 696-703, 2003.*

3D Boltzmann Simulation of the Io's Plasma Environment with Adaptive Mesh and Particle Refinement. A. S. Lipatov and M.R. Combi. *Icarus* (submitted), 2004.

Effects of kinetic processes in shaping Io's Global Environment: 3D hybrid and fluid-ion-particle-ion models of the Galileo I27 Flyby. A. S. Lipatov and M.R. Combi. *Icarus* (in preparation).

IV. References

Crifo, J. Inferences concerning water vapor viscosity and mean free path at low temperatures, Astron. Astrophys. 223, 365-368, 1989.

Combi, M. Time Dependent Gas Kinetics in Tenuous Planetary Atmospheres: The Cometary Coma, Icarus, 123, 207-226, 1996.

Combi, M.R., T.I. Gombosi, K. Kabin. Plasma Flow Past Cometary and Planetary Satellite Atmospheres, In *Atmospheres in the Solar System : Comparative Aeronomy, Geophysical Monograph 130,* 151-167, 2002.

Combi, M.R., K. Kabin, D.L. DeZeeuw, T.I. Gombosi, and K.G. Powell. Dust-Gas Interrelations in Comets: Observations and Theory. *Earth, Moon, & Planets* **79**, 275-306, 1997-1999.

Finson, M.L. and Probstein, R.F. A Theory of Dust Comets II. *Astrophys. J.* **154**, 353-380, 1968.

Gombosi, T., A. Nagy, T. Cravens, Dust and Neutral Gas Modeling of the Inner Atmospheres of Comas, *Rev. of Geophysics, Vol. 24, No. 3, 1086.*

Kitamura, Y., Axisymmetric dusty gas jet in the inner coma of a comet, *Icarus*, 66, 241–257, 1986.

Körösmezey, A., and T. I. Gombosi, A time-dependent dusty gas dynamic model of axisymmetric cometary jets, *Icarus,* 84, 118–153, 1990.

Lipatov, A.S. and M.R. Combi. Effects of kinetic processes in shaping Io's global plasmaenvironment: A 3D hybrid model. *Icarus* (submitted), 2004

Tenishev, V.M. and M.R. Combi. DSMC Simulation of the Cometary Coma. *Proceedings of the 23rd International Symposium on Rarefied Gas Dynamics*, Whistler, BC, July 20 - 25, 2002.

Tenishev, V.M. and M.R. Combi.Development of a General Purpose 3D DSMC Flow Solver on Unstructured Meshes. AIAA Paper 2003-3776, 2003.

Wallis, M. Dusty Gas-Dynamics in Real Comets. In *Comets*, Ed. L. L. Wilkening, U. Arizona Press, Tucson, AZ, 1982.

Development of a General Purpose DSMC Flow Solver on Unstructured Meshes (AIAA Paper 2003-3776, 2003)

V. Tenishev*, M. Combi†

Space Physics Research Laboratory, Department of Atmospheric, Oceanic and Space Sciences, University of Michigan, Ann Arbor, MI

Abstract

A general purpose kinetic parallel flow solver was developed based on DSMC methodology. Basic characteristics of the solver and some examples of its application are outlined in the paper.

Introduction

One of the most important aspects of the rarefied gas simulation is a high value of the Knudsen number $Kn = \lambda / L$ in the flow and, consequently, the requirement of solution of the Boltzmann equation

$$\frac{\partial f_i}{\partial t} + \mathbf{v}_i \nabla f_i + \frac{\mathbf{a}_i}{m_i} \nabla_v f_i = \left(\frac{\delta f_i}{\delta t} \right)_{coll} \quad (1)$$

The situation is usually more complicated because most of the practical applications involve consideration of diatomic gases, which can be excited vibrationally and rotationally and for which ionization, dissociation and chemical transformations are possible. A need to model non-equilibrium hypersonic flows motivated the development[1] of numerical techniques to treat such problems. Nowadays the DSMC method[2] is *de facto* the standard method for rarefied gas dynamics, where the state of the rarefied gas flow, which is presented by an assembly of molecules, is determined by collisional dynamics of a finite number of model particles and, hence, hold potential for providing information on flows where the collisional rate is not sufficient to maintain equilibrium energy distribution.

This paper presents the current status of development of a general purpose DSMC flow solver and some results of its application.

Code

Current problems of gas dynamics cannot be solved by methods other than numerical ones. A wide range of practically important problems requires developing a highly general numerical tool. C++ language was chosen in the present work.

Requirements

The following main principles guided the development of the code:

1. Portability: the code was tested on a set of different platforms and compilers.
2. Easy modification of the core of the code: change of the basic physico-chemical models installed into the code should not require any changes in any other part of the code.
3. Careful usage of resources: special attention has been paid to optimize allocation of memory and CPU resources.
4. Parallel implementation: MPI library has been used in parallelization of the system. Dynamic and static load balancing capabilities were implemented.
5. Easy adaptation of the code to particular physical problem (without modifacation of the core of the code).
6. Friendly user interface: easily understandable input and output files.
7. Pre/post-processing: including pre/post-processor into the core of the system,

---

* Research Assistant; vtenishe@umich.edu

† Senior Research Scientist

allow running and post-processing on different platforms.

8. Optimization of the numerical procedure for the current problem: change main parameters of simulation on order to improve overall performance.

Basic Specification of the System

The code potentially can be applied to a wide range of problems. The following is the list of its main features.

1. Neutral gas flow analysis in 1, 2, 3D cases. Spherical- and axis-symmetry can be taken into account.
2. The flow field is reconstructed on an unstructured mesh.
3. Multiple species gas flows can be modeled. Chemical reactions and relaxation of internal degrees of freedom can be considered.
4. A set of molecular and collisional models is available.
5. Mean free path and model particle weight adaptation has been implemented

Code Adaptation for Particular Problem

The core contains a general set of models (molecular models, collisional, chemical models). Some cases require introduction of additional particles or/and physicochemical models to solve particular problem. Such models may contain a set of approximations or/and experimental data specifically suited for the problem and, so, they may not be useful for any other cases. It is good to have the possibility to incorporate models into numerical procedure without any modification of the core of system. There are several difficulties that have to be solved in this way. Based on capabilities that are provided by C++, an approach of treating problem-dependent models was developed and incorporated into the system.

Optimization techniques

The accuracy of the numerical results, which are obtained by the DSMC method, is very dependent on the size of the sample and, finely, on the number of model particles per cell. So, in order to make the most effective use of computer resources, it is desirable to get the distribution of model particles over the domain close to uniform. This problem is especially important for the case of a 2D axisymmetrical simulation. There are several methods[2] to control the distribution of particles: variation of time steps, grid manipulation and direct variation of a particle's weight.

Several techniques could be used to decrease total computational cost of steady state simulation. Due to methodology of the DSMC method, a steady state solution can be obtained as the limit of unsteady flow simulation, where convergence takes a considerable part of total computation time. To get faster convergence, it is possible, starting with low accuracy, to improve it gradually as the current solution converges to the finial result. One of the possible implementations[3] of the strategy is to gradually increase total number of model particles as the flow pattern converges to the steady state. Another scheme was developed and implemented in the current work. The simulation is conducted on a set of meshes with different levels of refinement, starting with a coarse grid at the very beginning and maintaining the number of model particles per cell in desired limits. As the number of collisional cells and particles employed increase, the resolution of the computational procedure improves both in terms of flow macroparameters distribution and captured physical processes.

The use of parallel computers can significantly increase the range of application of the DSMC method. Effective use[4] of such computational systems can be achieved only with careful load balancing.

Static and dynamic load balancing capabilities are incorporates into the current implementation. Different criteria are available for the balancing. Static load balancing may be based either entirely on parameters of initial flow condition or on some knowledge about the structure of converged solution. In the first case, the load is balanced by equipartitioning of total number of particles, total volume or total cell number among all available processors. In addition to them, a total execution time can be used as a criterion in dynamic load balancing.

Applications of the code

Cometary Comae Simulation: Generic Jupiter Family Comet

The cometary atmosphere is a unique phenomenon in the solar system. It represents highly extended dusty gas cloud with a large range of change of its macroparameters from fluid to collisionless. So, kinetic methods are the most suitable tools for simulation processes in cometary comae.

PHYSICAL MODEL

When the nucleus approaches the sun, it absorbs solar radiation, resulting in an increase of gas sublimation from the surface. Because the gravitational force is negligible, the gases leaving the surface form a cometary exosphere. The radiation reaching the surface and supplying energy for sublimation is partially adsorbed dusty atmosphere. Any changes in the gas and dust production result in changes of optical characteristics of the cloud. The main volatile component of the cometary coma is water. So, water sublimation controls sublimation of others components when a comet is within about 4 astronomical units (AU) of the sun. Freshly evaporated molecules are photodissociated and photoionized, and therefore most of the chemical kinetics of cometary atmospheres involves the resulting highly reacting ions and radicals[5]. Most of the absorption of solar radiation takes place at the surface or in the dense region near the surface. Models of temperature and gas production distributions on the surface of a spherical nucleus can be found[6,7]. The simplest model of gas production assumes an optically thin coma, which is an excellent approximation for most comets, most of the time.

The conditions for a comet coma usually consider the gas at the surfaces to be stationary at a given temperature. This assumption neglects the real physics of the gas surface interface. But to get correct structure of the flow field in the near nucleus region, it is more important that the flux integrated around the surface equals the desired production rate and the gas temperature near the surface is close to vaporization temperature of water. Due to absence of gravity, the downward flux is negligible. This result in upward-half Maxwellian distribution of water vapor in a gas layer where thermodynamic equilibrium is not held. So, in a cometary atmosphere, unlike that of planets atmospheres, the mean flow velocity can be comparable with to the thermal speed[5], therefore methods adopted for studying planetary atmospheres are not longer valid. The flow then quickly thermalizes and passes smoothly through the sonic transition.

Two-dimensional axisymmetrical models for six species (H_2O, CO, OH, H_2, O, H) were considered in this work. A hard sphere collision model was assumed for intermolecular collisions. For water-water collisions the viscosity equivalent cross section[8] has been used. For other collision pairs, collision cross sections based on relevant atomic data were used[9].

The cometary nucleus was assumed to be spherical with a given radius and axisymmetrical gas emission. The gas flux from the dayside is controlled by absorption of solar radiation, and the flux is varying as the square of the cosine of the subsolar angle. It was assumed that only two gaseous species sublimate from the surface: H_2O and CO. Both species are in equilibrium with the surface and in the outflow mixture is partitioned on 80% for H_2O and 20% for CO.

Photochemistry is included into the model. The main reaction branches are presented in Table 1

Reaction	Branching ratio
$H_2O \rightarrow H+OH$	0.88
$H_2O \rightarrow H_2+O$	0.22
$OH \rightarrow O+H$	1.00
$H_2 \rightarrow H+H$	1.00

Table 1 Photochemical branching

STATEMENT OF THE PROBLEM

A comet with a production rate of 3×10^{28} molecules/sec was chosen, as typical of Jupiter family comets which will be spacecraft mission targets over the next decade or two. The radius of the nucleus was taken to be 10 km and the gas production rate was distributed as the square of the cosine of the subsolar angle with no gas emission on the night side. The gas was initiated at the surface at rest and with a temperature of 180K. The results of the calculation are shown in Fig. 1,2.

For photochemical reactions, the rates are typically much smaller than collision rates near the nucleus. Taking the characteristic time constant for particular photochemical reaction τ_i the probability of photodecay for a single molecule at a given time step Δt is

$$p_i = 1 - \exp\left(-\Delta t/\tau_i\right)$$

The regime of expansion of the cometary coma changes from collision dominated near the surface of the nucleus though transitional one to collisionless in the far field. Consequently, all of the regimes have to be described by numerical approach chosen for simulation, which makes questionable applicability of fluid based approximations.

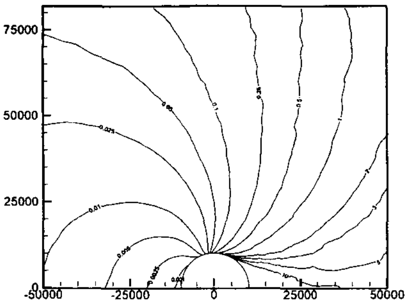

Fig. 1 The two-dimensional field of Knudsen numbers for the case of a generic Jupiter family comet.

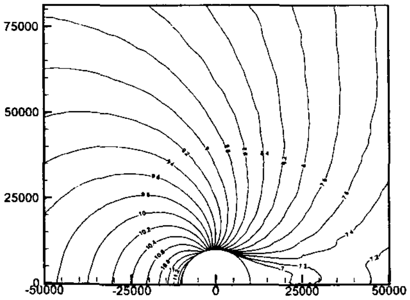

Fig. 2 The two-dimensional field of decimal logarithm of water density (in cm^{-3}) for the case of a generic Jupiter family comet.

Gas/Dust Interaction in cometary comae

Our present understanding of cometary nucleus is based on idea of "dirty snowball" according to which the nucleus consists of frozen volatiles and nonvolatile dust. The sublimated dust molecules drag away dust particles from the surface of cometary nuclei, so, the gas/dust interaction may a have significant effect on macroparameter distributions in comeraty comae. In this work, our particular interest was concentrated on modeling of inner comae processes, the region where dust and gas are produced and accelerated to their terminal velocities.

The following mechanism of dust particle acceleration is adopted here. It is assumed that an influence of gravitational force is negligible and, so, dust particles acceleration is only due to collisions with the gas molecules

Different kinds of gas molecules/dust surface interaction mechanisms can be easily introduced into the model, the simplest version of which assumes elastic reflection on the surface of the dust particle. In the current work, its simplified approximation has been used. Taking a as the dust particle radius, V_{dust} and V_{mol} as dust and gas particle's velocities, the change in momentum of the dust particle during time interval Δt can be expressed as

$$\Delta M_{dust} =$$

$$= \Delta t \sum_{mol} 2\pi a^2 m_{mol} \left|V_{mol} - V_{dust}\right| \left(V_{mol} - V_{dust}\right) \frac{F_{mol}}{V_{cell}}$$

Here, F_{mol} is the model particle weight of gas molecule and V_{cell} the volume of the computational cell. The model has been validated via comparison with test solution obtained by a fluid/dust model[5]. For the problems of cometary comae simulation, due to a wide range of collisional regimes in the flow, application of the fluid approximation is restricted.

The problem was considered in 1D spherically symmetrical geometry. The nucleus radius $R = 5.3 km$ and gas production rate of 3.5×10^{28} molecules/s corresponds to parameters of comet Borrelly at heliocentric distance of 1.36 AU. It was assumed that only H_2O molecules are sublimates from the surface. The dust/gas mass ratio is 0.4.

Some obtained results are shown in Fig. 3, 4.

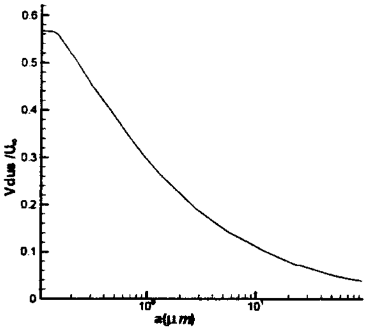

Fig. 3 Dust particles terminal velocity profile as the function of its radius. Here U_∞ is the terminal velocity of the gas phase.

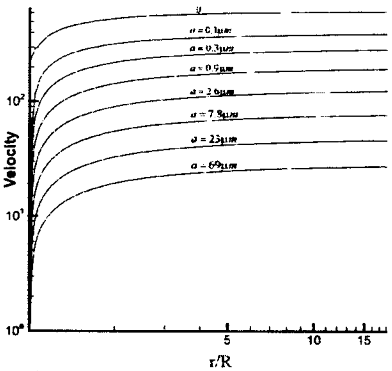

Fig. 4 Radial mean velocity (m/s) profiles for dust particles of a given size and the gas phase in the cometary coma as a function of a distance from the nucleus.

3D Two Body Interaction Problems

The ultimate goal of the work is developing of a general purpose DSMC flow solver that can be used to solve a wide range of problems in complex geometries. A two-body interaction problem has been chosen to demonstrate the capability of the code to treat complex 3D flow problems. The geometry of the problem is presented on the Fig. 5.

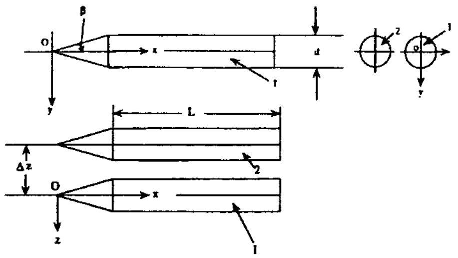

Fig. 5 Geometry sketch for the 3D two body interaction problem

Two bodies of revolution are cone/cylinder combination. The cone semi-angle is $\beta = 20^\circ$, the cylinder length is $L = 250mm$, its diameter is $d = 50mm$. The distance between the body axes is $\Delta z = 70mm$. The bodies of revolution were aligned parallel, without relative displacement at a zero incidence angle.

The flow of N_2 has been simulated on a mesh with 5.7×10^6 computational cells using $\sim 70\times10^6$ model particles. The upstream conditions are, $U_\infty = 1242.6m/s$, $T_\infty = 51K$, $n_\infty = 8.95\times10^{21}$, which corresponds to Mach number of M=9.91. Some of the results are presents of Fig. 6, 7.

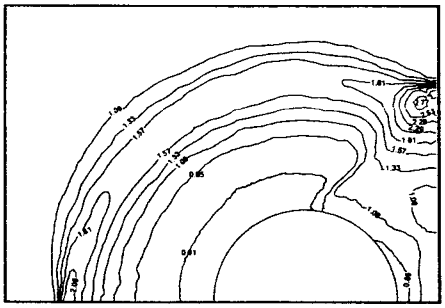

Fig.6 Normalized number density profile at a distance of 0.67L from the leading edge of the body

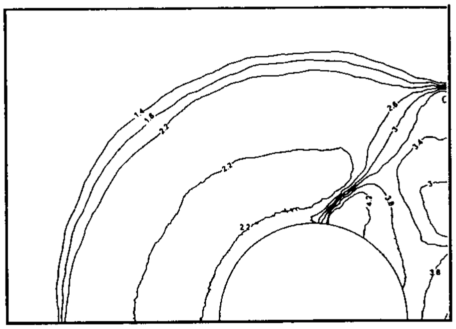

Fig. 7 Normalized temperature profile at a distance of 0.67*L* from the leading edge of the body

Conclusion

The current state of developing a general-purpose kinetic flow solver was presented. The tool has been validated via comparison with solutions of a set of test problems.

Main features of the code were outlined. It was stressed that portability, modularity, easy adaptation to particular problem, parallel implementation and friendly user interface makes the developed code a useful tool for analysis of complex multidimensional gas flows of chemically reactive mixtures. Discretization of the flow field on unstructured meshes allows the code to be used for solution of problems of internal and external gas flow in the case of complex geometries. Adaptation capabilities can be utilized to optimize overall performance.

In the paper, some examples of application of the code have been presented. A problem of two-phase dust/gas flow has been considered.

References

1. G. Bird, *Molecular Gas Dynamics and the Direct Simulation Monte Carlo Method,* Clarendon Press, 1994
2. G.N. Markelov, A.N. Kudryavtsev, M.S. Ivanov, *Continuum and Kinetic Simulation of Shock Wave/Laminar Boundary Layer Interaction In Hypersonic Flows,* AIAA-99-3527
3. M. Ivanov, G. Markelov, S. Gimelshein, *Statistical Simulation of Reactive Rarefied Flows: Numerical Approach and Applications,* AIAA 98-2669
4. S. Dietrich, I. Boyd, *Scalar and Parallel Optimized Implementation of the Direct Simulation Monte Carlo Method,* J. Comp. Physics, 126(2):328-342, 1996
5. T. Gombosi, A. Nagy, T. Cravens, *Dust and Neutral Gas Modeling of the Inner Atmospheres of Comas*, Rev. of Geophysics, Vol. 24, No. 3, 1086
6. A. Enzian, J. Klinger, G. Schwehm, P. Weissman, *Temperature and Gas Production Distributions on the Surface of a Spherical Model Comet Nucleus in the Orbit of 46P/Wirtanen*, Icarus **138**, 74–84 (1999)
7. P. Gutiérrez, J. Ortiz, R. Rodrigo, J. López-Moreno, *A study of water production and temperatures of rotating irregularly shaped cometary nuclei*, Astron. Astrophys. 355, 809-817 (2000)
8. J. Crifo, *Inferences concerning water vapor viscosity and mean free path at low temperatures*, Astron. Astrophys. 223, 365-368(1989)
9. M. Combi, *Time Dependent Gas Kinetics in Tenuous Planetary Atmospheres: The Cometary Coma*, Icarus, 1236 207-226 (1996)

Effects of kinetic processes in shaping Io's global plasma environment: A 3D hybrid model

Alexander S. Lipatov[1,2], and Michael R. Combi[1]

[1] Space Physics Research Laboratory, Department of Atmospheric, Oceanic and Space Sciences, The University of Michigan, Ann Arbor, MI 48109-2143

[2] also Dialogue-Science, Computing Center Russian Academy of Sciences, Vavilova St. 40, 119991 Moscow, Russia

Number of pages - 42

Number of figures - 20

Number of tables - 1

Corresponding author: A. S. Lipatov, Space Physics Research Laboratory, Department of Atmospheric, Oceanic and Space Sciences, The University of Michigan, Ann Arbor, MI 48109-2143, Phone: (734) 763-6246, FAX: (734) 647-3083 email: alipatov@engin.umich.edu

Short title: IO'S PLASMA ENVIRONMENT

Abstract. The global dynamics of the ionized and neutral components in the environment of Io plays an important role in the interaction of Jupiter's corotating magnetospheric plasma with Io. The stationary simulation of this problem was done in the MHD and the electrodynamics approaches. **One of the main significant results from the simplified two-fluid model simulations (Saur et al., 2002) was a production of the structure of the double-peak in the magnetic field signature of the I0 flyby that could not be explained by standard MHD models. In this paper, we develop a method of kinetic ion simulation.** This method employs the fluid description for electrons and **neutrals** whereas for ions multilevel, drift–kinetic and particle, approaches are used. **We also take into account charge-exchange and photoionization processes. Our model provides much more accurate description for ion dynamics and allows us to take into account the realistic anisotropic ion distribution that cannot be done in fluid simulations.** The first results of such simulation of the dynamics of ions in the Io's environment are discussed in this paper.

KEYWORDS: Io; Jupiter; Magnetosphere; Satellites; Atmospheres.

1. Introduction

The global interaction of the Jovian plasma torus with the Io is a fundamental problem in magnetospheric physics. It requires the solution of a highly nonlinear coupled set of integro-MHD/kinetic-Boltzmann equations which describe the dynamics of Jupiter's corotating magnetospheric plasma, pickup ions and the ionosphere together with the atoms from Io's environment. To leading order, the plasma and neutral atoms are coupled by resonant charge exchange, although other coupling processes are present. The characteristic scale of the ionized components is determined usually by the typical ion gyroradius, which for Io is much less than characteristic global magnetospheric scales of interest. By contrast, the mean free path of neutral particles and the typical ion gyroradius are comparable to characteristic exospheric scales such as the thickness of the exosphere and atmosphere, the distances separating the possible magnetic barriers and the surface of Io, etc. Consequently, the Knudsen number $Kn = \lambda / L_{exo}$ (λ, the mean free path of neutral particles and L_{exo}, a characteristic exospheric scale), which is a measure of the distribution relaxation distance, satisfies $Kn \approx 1$. Thus it is difficult to assume that the distribution of the neutral atoms and ions can relax to a Maxwellian distribution, and one needs ideally to solve a Boltzmann equation for the neutral and ionized components in which charge exchange and photoionization processes are included.

Several approaches for including the neutral component and pickup ions self-consistently in models describing the interaction of plasma torus with Io have been formulated. Early theoretical work was often done either in the context of a "thin" atmosphere (e.g., see Cloutier et al., 1978) indicative of the surface temperature (130 K), or "thick" extended neutral atmosphere (e.g., see Goertz, 1980) more indicative of volcanic temperatures (1000K). Subsequent evidence (see the review by Lellouch, 1996) seems to indicate a mixed picture of the global atmosphere, which has a large extended corona like a thick atmosphere, but appears to be dominated by local major injection of hot (high speed) gas/dust plumes to high altitudes but only near active volcanic vents. Therefore, although the atmosphere is probably only locally thick, it still has a large extended neutral corona which might provide a sufficient source of impact ionization and photoionization to explain the plasma torus.

Southwood et al. (1980) examined data from several Voyager instruments and examined the possible role of an intrinsic magnetic field for Io as a way to retain a robust enough ionosphere, which could provide enough conductivity for completing the Io-Jupiter current circuit. **Neubauer (1980) presented an analytical model of the Alfvén standing wave current system which connects current through the ionosphere of Io.** Southwood and Dunlop (1984) and Ip (1990) suggested models stating that mass loading effects should result in the formation of a tail-like structure in the wake behind Io; as a consequence of the enhanced plasma density, the magnetic field perturbations are continued into the wake. Thus the field-aligned current is not only generated by Io itself, but also in the wake. Several years after Voyager, 3D numerical studies of the plasma flow past Io were performed using electrodynamic (Wolf-Gladrow et al., 1987), magnetohydrodynamic (Linker et al. 1989; Linker et al. 1991) and resistive magnetohydrodynamic (Kopp, 1996; Kopp, Birk and Otto, 1998) approaches.

There have been recent efforts to improve and extend the pre-Galileo simulations both in terms of the MHD (Combi et al., 1998; Linker et al., 1998; Kabin et al., 2001) and the electrodynamic (Saur et al., 1999) approaches. These two approaches are distinguished by the physical assumptions which they each do and do not (or in some cases, can and cannot) include. However, MHD cannot, at least yet, include the effects of realistic conductivities (Hall and Pederson) or charge separation effects which are likely to be important very close to Io where the neutral densities are large and electric potential can introduce non-symmetric flow around body. They either include constant artificial conductivity (Linker et., 1998) or assume perfect conductivity (Combi et al., 1998), however comparisons of the sets of published results do not indicate that this choice has any important consequence.

The non-magnetic models produce magnetic field perturbations that are similar to the Galileo measurements, but none are quite as deep or as broad, and none have the reversal of the perturbation (the double-peaked structure) in the center of the wake. The magnetized models of Linker et al. (1998) produced a broad and deep perturbation, but not the self-reversal at the center of the wake (the double-peak or bite-out). Thus, the observational data, e.g., density and magnetic field profile along the Galileo trajectory cannot be fully explained by MHD models. But the most recent evidence from all the Galileo flyby data is that Io does not possess any substantial internal magnetic field of its own (Kivelson et al., 2001).

In the electrodynamical model of Saur et al. (2002), they added an extra ionization source, based on the high-energy bidirectional electrons observed by Williams et al.

(1996,1999) and Frank and Paterson (1999). These high-energy electrons were included as an energy source in addition to electron impact ionization by the thermal electrons and photoionization to create a dense plasma wake as is observed. Simulations without these extra bidirectional electrons show a nearly empty wake Saur et al. (1999). They also concluded that the electrodynamic part of Io's interaction is best described as an ionosphere-like interaction rather than a comet-like interaction (Saur et al., 2003). **Saur et al. (2002) demonstrated first that the diamagnetic and inertia currents are responsible for formation of the double-peak magnetic profile along the IO trajectory. They received the magnetic field profile that has an oscillating structure and the maximum in the magnetic field profile is to some extend was a narrower than in observation for standard model of the atmosphere (Fig. 11, Saur et al., 2002). In a case of longitudinally symmetric atmosphere they received a strong double-pick structure but the spatial scale of this structure was a twice smaller than in observation (Fig. 14, Saur et al., 2002) and the space scale of these peaks are much smaller than in observation.**

In this paper, we describe a new approach to solving the time-dependent Boltzmann equation together with a hybrid plasma (ion kinetic) model in three spatial dimensions using a prescribed atmosphere model for Io. A Boltzmann simulation is applied to model charge exchange between (incoming and pickup) ions and immobile atmosphere. Several simulations are run, and the results described. We show for the first time the predicted distribution for ions and the electromagnetic field throughout Io's environment. The results of such kinetic simulations are compared with those obtained from a related

MHD model and observational data. We also found the best parameters for our model that describe satisfactory the main behavior of the observational data at least on the qualitative level.

2. Formulation of the Problem and Mathematical Model

2.1. Simulation Model

To study the interaction of the plasma torus with the ionized and neutral components of Io's environment we use quasineutral hybrid models for ions and electrons. The interaction of the ions with atmosphere is dominated by charge exchange. The atmosphere is considered to be an immobile component in this paper. The general scheme of the global interaction of the plasma torus with Io and the Galileo I0 trajectory is given in Fig. 1. The Galileo I0 flyby occurred nearly in the equator plane of Io and perpendicular to the direction of the plasma wake defined by the corotating plasma flow past Io. The spacecraft trajectory passed approximately 900 km down-stream of Io (in the sense of the plasma torus flow). In our coordinate system the Z axis is parallel to U_0 (corotational plasma velocity), Y is aligned with the spin axis, and $\mathbf{X} = \mathbf{Y} \times \mathbf{Z}$. The relation between our coordinate system and IphiO (X^*, Y^*, Z^*) system (see Fig. 3 from Kivelson et al., 2001) is the following: X is parallel to Y^*, Y is aligned with Z^*, and Z is parallel to X^*.

In the hybrid simulations described here, the dynamics of upstream ions and implanted ions is described in a kinetic approach, while the dynamics of the electrons is described in a hydrodynamical approximation.

The single particle ion distribution function $f_s(t, \mathbf{x}, \mathbf{v})$ has to fulfill the Vlasov equation

$$\frac{\partial}{\partial t} f_s + \mathbf{v} \frac{\partial}{\partial \mathbf{x}} f_s + \frac{\mathbf{F}}{M_s} \frac{\partial}{\partial \mathbf{v}} f_s = 0 \tag{1}$$

where **F** symbolizes all forces acting on the ions.

The single ion particle motion is described by the equations

$$\frac{d\mathbf{r}_{s,l}}{dt} = \mathbf{v}_{s,l}; \quad \frac{d\mathbf{v}_{s,l}}{dt} = \frac{Z_s e}{M_s}\left(\mathbf{E}^* + \frac{\mathbf{v}_{s,l} \times \mathbf{B}}{c}\right), \quad \mathbf{E}^* = \mathbf{E} - \sigma_{eff}^{-1}\mathbf{J}. \tag{2}$$

Here Z_s and M_s denote the charge state and the mass of the ions, the subscript s denotes the ion species ($s = 1$ for incoming ions and $s = 2$ for pickup ions) and the index l is the particle index. σ_{eff} is an effective conductivity that may include Coulomb collisions and collisions due to particle-wave interaction, in the sense of a standard resistive Ohm's law. Note that the resistivity used in Eq. (2) must depend on individual velocities of ions and electrons. However, we use the effective resistivity and an effective electric field E^* in Eq. (2) to satisfy momentum conservation for the plasma system (Zueva et al., 1975).

In the nonradiative limit Ampère's law is given by

$$\frac{4\pi}{c}\mathbf{J} = \nabla \times \mathbf{B}; \tag{3}$$

and the induction equation (Faraday's law) by

$$\frac{1}{c}\frac{\partial \mathbf{B}}{\partial t} + \nabla \times \mathbf{E} = 0. \tag{4}$$

The total current is given by

$$\mathbf{J} = \mathbf{J}_{\mathrm{e}} + \mathbf{J}_{\mathrm{i}}; \quad \mathbf{J}_{\mathrm{i}} = \sum_{s=1}^{2} Z_s e n_s \mathbf{U}_s, \tag{5}$$

here $\mathbf{U}_s$ is the bulk velocity of ions of the type s.

We further assume quasi-neutrality

$$n_\mathrm{e} = \sum_{s=1}^{2} Z_s n_s. \tag{6}$$

For massless electrons the equation of motion of the electron fluid takes the form of standard generalized Ohm's law (e.g. Braginskii, 1965):

$$\mathbf{E} = \frac{1}{e n_\mathrm{e} c}(\mathbf{J}_\mathrm{e} \times \mathbf{B}) - \frac{1}{e n_\mathrm{e}} \nabla p_\mathrm{e} + \frac{1}{e n_\mathrm{e}} \mathbf{R}_\mathrm{e}, \tag{7}$$

where $p_\mathrm{e} = n m_\mathrm{e} \langle v_\mathrm{e}'^2 \rangle / 3 = n_\mathrm{e} k_B T_\mathrm{e}$, and v_e' are the scalar electron pressure and the thermal velocity of electrons, and the electron current is estimated from Eq. (5).

The term including $\mathbf{R}_\mathrm{e}$, symbolizes the mean momentum change of the electrons due to their collisions with the ions, which can be parametrized in terms of the collision frequency ν_{es} between electrons and ions of the species s as

$$\mathbf{R}_\mathrm{e} = -n_\mathrm{e} m_\mathrm{e} \nu_\mathrm{es} (\mathbf{U}_\mathrm{e} - \mathbf{U}_\mathrm{s}) \tag{8}$$

Since we suppose that electron heating due to collisions with ions is very small, the electron fluid is considered adiabatic:

$$p_\mathrm{e} \propto n_\mathrm{e}^{5/3}. \tag{9}$$

The ion kinetic approach allows us to take into account the effects of anisotropy of ion pressure, the correct mass loading processes, a penetration of ions across the ionosphere, and the asymmetry of plasma flow around the Io. Remember that the fluid models which account only for the scalar ion pressure may result in an extra-effusion of the pickup ions along the Alfvén wing.

Charge exchange may be included in a hybrid model by a simple procedure (Lipatov et al., 1998; Lipatov, 2002). The total loss rate in s^{-1} for the ionized component has the form

$$\beta_{\text{ex}}(\mathbf{x},\mathbf{v},t) = \int f_a(\mathbf{x},\mathbf{v}_a,t) V_{rel,a} \sigma_{ex}(V_{rel,a}) d^3\mathbf{v}_a, \tag{10}$$

where the velocity of ions relative to an atom with velocity $\mathbf{v}_a$ is $V_{rel,a} = |\mathbf{v} - \mathbf{v}_a|$.

If we suppose that the neutral component has a Maxwellian distribution, then β_{ex} may be approximated as (Ripkin and Fahr, 1983)

$$\beta_{\text{ex}}(\mathbf{x},\mathbf{v},t) \simeq n_a(\mathbf{x},t) V_{rel,a} \sigma_{\text{ex}}(V_{rel,a}). \tag{11}$$

In this paper we assume that the neutral component of Io's atmosphere has zero bulk and thermal velocities. If one needs to include the nonzero temperature and bulk velocity, the effective average velocity of ions relative to an atom with velocity may be found from the general equation of Ripkin and Fahr (1983).

Let the time interval t^* with respect to the charge exchange be a random variable with a distribution function

$$w_l(t^*) = \exp[-\int_{t_0}^{t^*} \beta_{\text{ex},l} dt], \tag{12}$$

where l is the particle index.

A survival probability against the charge exchange event w_{ex} may be written as follows:

$$w_{\text{ex},l}(t) = \exp[-\int_{t_0}^{t} \beta_{\text{ex},l} dt]. \tag{13}$$

The integration is over the trajectory of the particle with index l. At the time of creation (either at the boundary of the calculation box, or at the moment of charge exchange), an ionized particle has initial coordinates $\mathbf{x}_l(t_0) = \mathbf{x}_{l,0}$, $\mathbf{v}_l(t_0) = \mathbf{v}_{l,0}$, a weight $\alpha_l(t_0) = \alpha_{l,0}$, and a survival probability $w_{\mathrm{ex},l}(t_0) = 1$. For each new ion with index l, we have to determine the critical probability $w^*_{ex,l}$ when charge exchange will occur, and this is done using the relation

$$w^*_{\mathrm{ex},l} = \xi, \tag{14}$$

where ξ is random number on the interval from 0 to 1. During the calculation we have to identify those particles for which the probability of survival satisfies the condition

$$w_{\mathrm{ex},l} \leq w^*_{\mathrm{ex},l}. \tag{15}$$

If the particle satisfies the condition (15), then we have to exchange the velocity of this ion with the velocity of an atom from the atmosphere of Io. In the present simulations, we do not take the cross section σ into account in (10) because of the weak dependence on $|v - v_p|$ (as was done in the work of Malama (1991)). If charge exchange occurs, then a new neutral particle begins its motion with $\mathbf{v}_l = 0$ and $w_{\mathrm{ex},l} = 1$.

Io's environment model includes 2 sources of pickup ions: the extended coma halo distribution with pickup ion production law

$$G \propto \nu_i n_{\mathrm{atmos}} W_{ext} r^{-2} \tag{16}$$

for $1 \times r_{\mathrm{Io}} < r < 7 \times r_{\mathrm{Io}}$ and the exosphere distribution close to Io with ion production law

$$G \propto \nu_i n_{\mathrm{atmos}} W_{int} \exp[-(r - r_{\mathrm{Io}})/H_{\mathrm{atmos}}]. \tag{17}$$

Here W_{ext} and W_{int} denote the fraction of the total ion production rate in the halo and exosphere ($W_{int} = (100 - 95)\%$ of the total), respectively. $n_{\rm atmos}$ **denotes the maximum atmosphere density,** ν_i **is effective ionization rate.**

The inner region of the Io's ionosphere is described by immobile ions with the following density distributions:

$$0.5 n_{\rm iono} \exp(-(r - r_{\rm Io})/H_{eff}), \quad \text{for} \quad r > r_{\rm Io},$$

$$n_{\rm iono}(1 - 0.5 \exp(-|r - r_{\rm Io}|/H_{eff})), \quad \text{for} \quad r < r_{\rm Io},$$

We assume that the incoming flow has a small finite resistivity to suppress the "shot" noise fluctuations. We also take into account the effect of finite conductivity of Io's body so that

$$\sigma_{eff} = \sigma_{\rm up}, \quad \text{for} \quad r > r_{\rm Io},$$

$$\sigma_{eff} = \sigma_{\rm Io}, \quad \text{for} \quad r \leq r_{\rm Io},$$

Our code solves equations (1) - (8), (5) - (9), (10) - (15) and (16) - (17).

Initially the computational domain contains only supersonic plasma torus flow with a homogeneous spatial distribution and a Maxwellian velocity distribution; the pickup ions have a weak density and spherical spatial distribution. The magnetic field and electric fields are $\mathbf{B} = \mathbf{B}_0$ and $\mathbf{E} = \mathbf{U}_0 \times \mathbf{B}_0$. Inside the Io electromagnetic fields are $\mathbf{E} = 0$ and $\mathbf{B} = \mathbf{B}_0$. In the cases examined in Figs. 9-16 we choose $\mathbf{B}_0/B_0 = (0, 1, 0)$; $\mathbf{E}_0/E_0 = (1, 0, 0)$ and in the cases examined in Figs. 2-8, 17-19 we choose $\mathbf{B}_0/B_0 = (0.0394, -0.9854, 0.1657)$ and $\mathbf{E}_0/E_0 = (-0.98, -0.0394, 0.0)$.

At $t > 0$ we begin to inject the pickup ions with a distribution according to Eqs. (16-17). Far upstream ($z = -DZ/2$), the ion flux is assumed to have a Maxwellian distribution,

$$f = n_\infty(\pi v_{th}^2)^{-3/2}\exp\left[-\frac{(\mathbf{v}-\mathbf{U})^2}{2v_{th}^2}\right], \tag{18}$$

where v_{th} and $\mathbf{U}$ are the thermal and the bulk velocities of the plasma torus flow, respectively.

Far downstream, we adopt a free escape condition for particles and Sommerfeld's radiation condition for the magnetic field. On the side boundaries ($y = \pm DY/2$ and $x = \pm DX/2$), periodic boundary conditions are imposed for incoming flow particles and the electromagnetic field. In some cases we also tested the use of the upstream boundary condition for electromagnetic field on the side boundaries. In these situations we also employ a buffer zone with thickness about of $10 \times \Delta x$ where a smoothing procedure provides a transition for electromagnetic fields from the perturbed value to the upstream value on the side boundaries (see e.g. Umeda et al., 2001), effectively allowing Io-generated Alfvén disturbances to propagate away. The pickup ions come out from the computational domain when they intersect the surfaces $x = 5 \times \Delta x$, $x = DX - 5 \times \Delta x$, $y = 5 \times \Delta y$, $y = DY - 5 \times \Delta y$, $z = 5 \times \Delta z$, $z = DZ - 5 \times \Delta z$. Thus the flux of the pickup ions is absent on the side boundaries. At Io's surface the particles may be reflected or absorbed. Note that the position of the Io is $x = 0, y = 0, z = 0$.

The three-dimensional computational domain has the dimensions $DX = 20L$, $DY = 20L$, and $DZ = 10L$, or $DX = 14L$, $DY = 14L$, and $DZ = 12L$, or $DX = 10L$, $DY = 10L$, and $DZ = 8L$, where L equals the radius of Io, $r_{\mathrm{Io}} = 1800\,\mathrm{km}$. We use the meshes of $201 \times 201 \times 101$, or $161 \times 161 \times 121$, or $141 \times 141 \times 121$ grid points, and 2×10^8

and 5×10^7 particles for ions and pickup ions, respectively, for a homogeneous mesh computation. The time step Δt satisfies the condition $v_{max}\Delta t \leq \min(\Delta x, \Delta y, \Delta z)/8$.

The relationship between dimensional (U, E, B, p_e, n, T) and dimensionless (U', E', B', p'_e, n', T') parameters may be expressed via dimensional upstream values as follows:

$$\mathbf{U} = \mathbf{U}'U_0, \quad \mathbf{E} = \mathbf{E}'B_0U_0/c, \quad \mathbf{B} = \mathbf{B}'B_0, \quad p_e = p_{e'}p_{e0},$$
$$n = n'n_0, \quad T = T'M_iU_0^2, \tag{19}$$

whereas the dimensional time and distance may be expressed via the bulk velocity U_0 and characteristic scale L:

$$t = t'L/U_0, \quad x = x'L. \tag{20}$$

2.2. Numerical Method

We employ a standard particle-in-cell (PIC) method in the case of a homogeneous grid. The time integration of the particle motion equations uses a leapfrog scheme. The time integration of the electromagnetic field equations uses an implicit finite difference scheme (see, e.g., Lipatov (2002)). We use different time steps for particle and field pushing (subcycling). This code was optimized for parallel computation using MPI and OMP.

Since the gyroradii must be resolved, a grid point spacing of less than 1 gyroradius is required in order to avoid numerical dispersion and dissipation. On the other hand, good statistics are required, therefore a sufficiently large number of particles per cell have to be used (i.e. low "shot" noise). We use a homogeneous mesh for the simulations presented here.

3. Results of the Simulation

To study the interaction of the plasma torus with the ionosphere of Io the following set of Jovian plasma torus and ionosphere parameters were adopted in accordance with observational data (Frank et al., 1996; Kivelson et al., 1996): corotation velocity, $U_0 = 56.8\,\mathrm{km/s}$; plasma density, $n_0 = 3500\,\mathrm{cm}^{-3}$; plasma temperature, 92 eV; mean ion mass, $M_\mathrm{i} = 22M_\mathrm{p}$; ratio of specific heats, $\gamma = 5/3$; ion and electron betas, $\beta_\mathrm{i} = 0.039$; $\beta_\mathrm{e} = 0.0022$; magnetic field, $B = 1800\,\mathrm{nT}$; Alfvén and sonic Mach numbers $M_\mathrm{A} = 0.4$ and $M_\mathrm{S} = 2.2$.

For pickup ions we use the following parameters: total ion production rate, $Q_\mathrm{ion} = (0.7 - 2.) \times 10^{28}\,\mathrm{s}^{-1}$; mean ion mass, $M_\mathrm{PI} = 22M_\mathrm{p}$; electron exosphere and ionosphere betas, $\beta_\mathrm{e,exo} = 0 - 0.0022$, $\beta_\mathrm{e,iono} = 0 - 0.0005$; effective cross section for charge exchange, $\sigma_\mathrm{exch} = 1.5 \times 10^{-15}\,\mathrm{cm}^2$; effective ionization rate, $\nu_i = 10^{-5}\,\mathrm{s}^{-1}$; atmosphere scale height, $H_\mathrm{atmos} = 0.06 - 0.09 \times r_\mathrm{Io} = 108\,\mathrm{km} - 162\,\mathrm{km}$; maximum value of the density of the atmosphere, $n_\mathrm{atmos} = (0.5 - 10) \times 10^8\,\mathrm{cm}^{-3}$; effective ionosphere scale height, $H_{eff} = (0.0001 - 0.00025) \times r_\mathrm{Io} =(0.18\text{–}0.45)\,\mathrm{km}$. Note that in calculation the effective ionosphere scale height is smoothed over the nearest grid cell and its specific values is not crucial. However, for charge exchange between the ions and atoms we use the analytical formula for the density of the atmosphere without any smoothing. The effective dimensionless diffusion length of the upstream and ionosphere plasmas is $l_\mathrm{d,up} = 0.00125$, whereas for Io's body the diffusion length is $l_\mathrm{d,Io} = 0.0125$, where

$l_\mathrm{d} = 1/Re$ and the magnetic Reynolds number is $Re = 4\pi U_0 L \sigma_{eff}/c^2$. The average Lunquist number for the ionosphere may be estimated as

$$Lq = \frac{\tau_{dif}}{\tau_\mathrm{A}} = \frac{Re}{M_\mathrm{A}},$$

where the characteristic diffusion and Alfvén times are $\tau_{dif} = 4\pi\sigma L^2/c^2$ and $\tau_\mathrm{A} = L/v_\mathrm{A}$. Note that Linker et al. (1998) used the following Lundquist number, $Lq = 500 - 1000$, magnetic Reynolds number, $Re = 200 - 400$ and diffusion length, $l_\mathrm{d} = 0.00125$ for the background plasma. This value of the diffusion length corresponds to an effective conductivity of about $1.2 \times 10^8\,\Omega^{-1}\mathrm{m}^{-1}$ far in upstream. Since many plasma and atmosphere parameters are still uncertain we have to study a wide spectrum of simple models in order to choose the best one for interpretation of the observational data. We can present here only a sample of the wide spectrum simulation results which are in agreement or in disagreement with observations in order to illustrate the dependence of the plasma environment near Io on the input parameters of the problem. The global structure of Io's environment is determined by a set of dimensionless independent parameters such as M_A, β_p, β_e, $M_\mathrm{PI}/M_\mathrm{p}$, ion production and charge exchange rates, diffusion lengths, and the ion gyroradius $\epsilon = \rho_\mathrm{ci}/L$. For real values of the magnetic field the value of the ion gyroradius is about 8 km **which is calculated by the use of the local bulk velocity.** The dimensionless ion gyroradius and grid spacing have the values $\epsilon = 0.0045$ and $\Delta_x/L = 0.1$. In order to study the ion kinetic effect we have to resolve the ion gyroradius on the grid. For this reason we use the artificially increased value of this parameter, $\epsilon = 0.126$, that is about of a value of Δ_x/L now. Although, such way allows us to study the some kinetic effects for realistic physics we have to extrapolate our results into a realistic scale. By scaling the gyroradius in such a way, we preserve the ratio of M_A, M_S, β_p, β_e, and more importantly accurately preserve any anisotropy of the ion distribution function with respect to the magnetic field.

3.1. Global Structure of the Io's Environment

Let us consider first the global picture of the interaction of the plasma torus with Io in a case with an ionization rate $Q_\mathrm{ion} = 3.03 \times 10^{27}\mathrm{s}^{-1}$ **(run ceie2, Table 1)** and charge exchange of form $\frac{A}{r^2} + B \exp \frac{r - r_\mathrm{Io}}{H_\mathrm{atmos}}$. The maximum value of the atmosphere density is $n_\mathrm{atmos} = 5 \times 10^7\,\mathrm{cm}^{-3}$ and diffusion lengths are $l_\mathrm{d,up} = 0.00125$ and $l_\mathrm{d,Io} = 0.00125$. Figures 2 and 3 demonstrate the asymmetrical distribution of the torus plasma ion (top) and pickup ion density (bottom) in the x–z and y–z planes. One can see the increase of the incoming ion density upstream of Io. The pickup ion motion is determined mainly by the electromagnetic drift. The motion along the magnetic field is due to the thermal velocity and the gradient of the electron pressure. The asymmetrical distribution of the incoming ions in the y-z plane may be explained by an existence of the B_z component of the upstream magnetic field. The inclination of the magnetic field results in the asymmetrical boundary condition for ion dynamics (penetration and reflection) in the Io's ionosphere and the asymmetrical Alfvén wing. The incoming ions flow around the Alfvén wing so that only a small portion of the incoming flux penetrates the wing, resulting in a decrease in the incoming ion density. This effect is stronger in upper half-plane ($y > 0$) (Fig. 3, top) because the Alfvén wing has a stronger front transition in this region than in a lower half-plane. The pickup ion distribution, Fig. 3 (bottom), gives the correct value for the inclination of the Alfvén wing, 21-21.5 degrees. The density profile is a little bit disturbed near the side boundaries, however, this perturbation does not affect the region close to Io as discussed already. Figures 4 and 5 show the distribution of the electric and magnetic fields. The asymmetry of the distributions in **E** and **B** appears to be caused by finite gyroradius effects of incoming and pickup ions. A weak perturbation of the magnetic field was observed near the ionosphere of Io: compression of the magnetic field upstream and decompression in the plasma wake.

Figure 5 also shows the formation of a strong Alfvén (and whistler) wing in the direction of the magnetic field. The perturbation of the electric field inside the wings is very strong and it may affect ion dynamics so that particles flow around the wings. The formation of the Alfvén wing in a subalfvénic flow near Io was studied first analytically by Neubauer (1980). A excitation of a whistler wave near a plasma cloud was studied by using 3-D hybrid simulation in Lipatov (2002). The above wave propagation is closely connected with the generation of low frequency waves by the harmonic dipole (local source) in the magnetized plasma. The first analytical studies of these effects may be found, for example in (Van'yan and Lipatov, 1972, and references therein).

Figures 6 and 7 show the velocity arrows of incoming and pickup ion velocities. The incoming ions flow around the effective obstacle that is produced by pickup ions and the ionosphere. The pickup ions flow from the "corona" across the magnetic field due to electromagnetic drift whereas the motion along the magnetic field is determined by the thermal velocity of ions and the electron pressure. Figure 8 shows the two-dimensional cross section for total ion density in the x-y plane. One can see the asymmetry of distribution relative to the x-axis due to the angle between the bulk velocity and the magnetic field upstream and to the y-axis due to effects of the finite ion gyroradius.

3.2. Effect of Electron Temperature on the Plasma Environment

Our model takes into account the three characteristic electron temperatures that do not play any role in past MHD models: a) the temperature of electrons in the plasma torus, $T_{\mathrm{e,up}}$; b) the temperature of electrons that are created together with pickup ions, $T_{\mathrm{e,PI}}$; c) the temperature of electrons that are created with ions in the ionosphere, $T_{\mathrm{e,iono}}$. Note that in all cases discussed here the pickup ions are generated only in the exosphere, i.e $W_{ext} = 0$.

Let us consider the case (a). Figure 9 shows the one-dimensional cuts of the total ion density, temperature and magnetic field along the x-axis for $z = 1.5 \times r_{\mathrm{Io}}$ and $y = 0$. One can see two peaks in the distribution of the density, each of which has a width of about r_{Io} and maximum densities of about 4 and 6.5 relative to the upstream density. The depletion of the density at $x = 2L$ may be explained by the following. When the supersonic flow passes around the obstacle, a wake with a decreased density is formed. The simple example of a such void is presented by the lunar plasma wake. However, in our case an asymmetrical pickup ion high density obstacle provides an asymmetrical void in Io's plasma wake. The temperature profile has two peaks with maximum temperatures of about 2.3 and 0.7. These peaks do not correlate with the peak in density because the temperature of the ions is determined by the heated ions from the incoming flow and pickup ions. The magnetic field profile shows a decrease in the magnetic field with a minimum value of about 0.5 in the plasma wake and with some significant oscillations (Fig. 9). Figure 10 shows a two-dimensional cross section of the total ion density across the plasma wake ($z = 1.5 \times r_{\mathrm{Io}}$). One can see three strong maxima. This distribution is determined by finite gyroradius effects of ions.

If we take into account the temperature of electrons that are created with pickup ions (case (b)) the distribution of the ions in the plasma wake may be changed significantly. The one-dimensional total density profile has one peak with a value of about 8 (Fig. 11). The temperature profile has also one strong peak with a value of about 1.9 and the magnetic field has a depletion with a minimum value 0.7 (Fig. 11). Figure 12 shows a two-dimensional cross section of the total density across the plasma wake. One can see a strong peak narrow in x-direction and wide in y-direction.

In case (c), when the temperature of electrons inside the ionosphere is also taken into account, we have the following distribution of plasma parameters in the wake. Figure 13 shows one-dimensional cuts of the total density, temperature and magnetic field. The density profile has a wide peak with a thickness of about $4r_{\mathrm{Io}}$ and a peak value of $n \approx 6$. The temperature profile has a two-peak distribution. The value of the temperature at the two peaks is about 0.6 and 0.55. The peaks are separated by a distance of $4 \times r_{\mathrm{Io}}$. The magnetic field profile has a minimum at the plasma wake with $B = 0.55$ (Fig. 13). Figure 14 shows the two-dimensional cross section of the total density across the plasma wake. One can see a strong peak which is narrow in the y-direction and wide in the x-direction. By introducing cool electrons inside the ionosphere we are trying to account in an appropriate way for the cooling effect on electrons through electron-collisions close to Io.

Finally, we show the two-dimensional cuts of pickup ion density for all three cases, Fig. 15 (top, middle, bottom). One can see that the temperature of electrons which are created in different regions of Io's environment may affect strongly the pickup ion distribution. Figure 15 demonstrates the importance of the electron pressure in the region close to the Io.

In the case of the absence of pressure of pickup and ionospheric electrons, the interaction of the plasma torus ions with Io is strongly asymmetrical in the x-z plane due to the finite ion gyroradius. In the plasma wake a "space-mixing" of the pickup ions is observed that results in the formation of an asymmetrical tongue-type distribution in the x-z plane. The effusion of pickup ions in the y direction is also weak because of small values of Δp_e and the velocity of the pickup ions in y direction, Fig. 15, (top).

In the opposite case, when the gradient of the pressure of the pickup electrons and the pressure of ionospheric electrons cause a strong electrostatic field, the pickup ion density distribution in the x-z plane becomes more symmetrical and wider across the wake compared with the above case (cf. Fig. 15 (top) and (bottom)). The gradient of the electron pressure also causes a strong effusion of the pickup ions along the Alfvén wing (see, Fig. 15 (bottom) and (top)).

Finally, in the intermediate case when the pressure of ionospheric electrons is small the asymmetrical distribution of the pickup ion density with a strong effusion along the

Alfvén wing is observed, Fig. 15 (middle). So, we can conclude that the pressure of the pickup ions is responsible for effusion processes while the pressure of the ionospheric electrons is responsible for the formation of the symmetrical distribution with the maximum in density located near the (y=0) plane.

All three cases, (a), (b) and (c), demonstrate strong asymmetries in the distributions of pickup ion density, temperature and magnetic field in comparison with MHD and electrodynamic models.

3.3. Effect of Pickup Ion Injection Distribution on the Plasma Environment

To study the role of pickup ions from the halo we simulated Io's environment for cases when the ion production rate in the halo corresponds to $W_{ext} = 10\%$ and $W_{ext} = 30\%$ of the total (halo plus exosphere) ion production rate. Note that all other parameters are the same in these cases.

Figure 16 (solid line) presents one-dimensional cuts for density, temperature and magnetic field for $W_{ext} = 10\%$ and $\beta_{\mathrm{e,iono}} = 0.25\beta_{\mathrm{e}}$. The density profile has a maximum value of about $n \approx 7.2$ with a characteristic width of the peak of $3 \times r_{\mathrm{Io}}$, that is higher than the observational value, $n \approx 5.1$. The temperature profile shows a two-peak distribution. The maximum values in the peaks are $T/T_0 \approx 3$ and $T/T_0 \approx 2.1$ that correspond to the observational data (Frank et al., 1996; Kivelson et al., 1996). The distance between peaks is about $3 \times r_{\mathrm{Io}}$ that is a little bit wider than observed value, $2 \times r_{\mathrm{Io}}$. The magnetic field profile has a minimum value in the plasma wake of $B \approx 0.5$ that also corresponds the minimum value of the B_y in the observational data. Figure 16, (dotted line) shows the one-dimensional cuts for density, temperature and magnetic field for $W_{ext} = 30\%$ and $\beta_{e,iono} = 0.25\beta_e$. The density profile has a maximum value of about $n \approx 5.83$ with a characteristic width of the peak of $4 \times r_{\mathrm{Io}}$, which is a little bit wider than that in Fig. 16, (solid line) and is a little higher than observed. The temperature profile also shows a two-peak distribution. The maximum values in the peaks are $T/T_0 \approx 6.8$ and $T/T_0 \approx 2.4$. Note that the first maximum in the temperature is higher than observed (Frank et al., 1996; Kivelson et al., 1996). The magnetic field profile shows a minimum value of the magnetic field in the plasma wake $B \approx 0.56$ that corresponds the observational data.

3.4. Effect of Ionospheric Conductivity on the Plasma Environment

In the previous cases we have assumed a high conductivity for the ionosphere and Io's body. The realistic models of Io may include a conducting core, surrounded by a poorly conducting mantle (a Moon-like model), or Io may be considered as a poorly conducting body. In this section we shall model the Io as a poorly conducting body. Note that all other parameters in this case are the same as that shown in Fig. 16, (solid line) except the higher diffusion length. Figure 16 (dashed line) shows one-dimensional cuts for the density, temperature and magnetic field for the case with a diffusion length, $l_{d,iono} = 0.025$. **Note that the lines in Fig. 16 corresponds the simulation for different sizes of the computational domain.** The value of the peak density is about $n \approx 7.5$ with the same thickness of the peak, $\approx 3r_{\mathrm{Io}}$ as in Fig. 16, (solid line). The maximum values of the peak temperature, 3 and 2 are approximately the same as in Fig. 16, (solid line) (see Fig. 16, (dashed line)). However, the magnetic field profile shows much stronger field variation in the external region of the plasma wake than in Fig. 16, (solid line). The analysis of the magnetic field inside Io shows that the reduced conductivity ($l_{\mathrm{d,iono}} = 0.025$, Fig.18 (dashed line)) near ionosphere and inside Io may reduce the magnetic field inside Io by $20 - 40\%$ and the peak plasma density at the Galileo trajectory by 5% in comparison with the model with $l_{\mathrm{d,iono}} = 0.0025$).

3.5. Comparison with Galileo Observational Data

The result of the measurements by the particle and field instruments on the Galileo Orbiter during the December 1995 flyby of Io provided new and important information with which realistic simulations for the plasma interaction can be tested. Along that trajectory physical signatures of the wake were seen as a broad depression in the magnetic field (Kivelson et al., 1996), sharp peaks in the ion (Frank et al., 1996) and electron (Gurnett et al., 1996) densities, a slowing of the plasma in the core of the wake, a deep ion temperature decrease in the center of the wake, and a large (factor of 3) ion temperature rise in the flanks of the wake (Frank et al., 1996). The magnetic field perturbation was broader spatially than the density peak, and showed a double-reversed structure, whereby the perturbation (as defined by the difference from the outer Jovian B-field value) was actually weaker right near the close-approach point than it was somewhat adjacent to the center of the wake. For comparison of the our computational model with observation data we made a run with the following plasma parameters: $\beta_{\mathrm{e,PI}} = 0.125\beta_{\mathrm{e,up}}$, $\beta_{\mathrm{e,iono}} = \beta_{\mathrm{e,up}}$, $n_{\mathrm{iono}} = 100n_0$, $H_{\mathrm{atmos}} = 0.06r_{\mathrm{Io}}$, $W_{ext} = 5\%$, and

$l_{\rm d,up} = 0.00125$. The conductivity of Io is chosen so that $l_{\rm d,Io} = 0.0125$.

Let us consider first a case in the absence of charge exchange processes (case nce Table 1). The total ion production rate was $Q_{\rm ion} = 4.8 \times 10^{27}\,{\rm s}^{-1}$. Fig. 17 shows the comparison of plasma parameters and magnetic field components from the simulation model and observation along the Galileo trajectory (Pass I0). **Note that we used the interpolation of the grid values of the plasma parameters and the magnetic field into the position of Galileo spacecraft.** We can see that the density peak is slightly shifted to the right in comparison with observed one. The left peak in the temperature profile is a little bit narrower than the observed one while the right peak is a little bit higher than the observed one. The simulation yields a little bit smaller value of B_y at large x, $x >> r_{\rm Io}$, due to perturbation of the electromagnetic field in the region above ($y > 0$) and below ($y < 0$) the equatorial plane. Unlike the MHD models the hybrid model yields a B_y profile with reverse structure in the middle of the plasma wake. This type of behavior may be explained by the diamagnetic and accelerational drift currents in the plasma wake, which are modeled naturally in our kinetic description for ions. The maximum value of these currents is located near the equatorial plane in the boundary layer (interface) between the external plasma flow and pickup ions in the plasma wake. The B_z profiles in these simulations correspond very well to the observed data however the left maximum in the magnetic field is smaller than observed one. Unfortunately fluctuations in magnetic field components are not very small due to "shot" noise. So the lack in agreement between observed and computed values of B_x is probably just the result from less than perfect plasma simulation model ("shot" noise), and the simplified models of the ionosphere and Io's body.

Let us consider now the cases with a charge exchange rate that corresponds to the maximum value of the density of the atmosphere, $n_{\text{atmos}} = 10^8\,\text{cm}^{-3}$. We assume here that the charge exchange process is due to only the exponential part of the neutral atmosphere.

Fig. 18 (solid line) shows the comparison of plasma parameters and magnetic field components from our simulation model and the observations in the case with a total ion production rate, $Q_{\text{ion}} = 2.27 \times 10^{27}\,\text{s}^{-1}$. In this case the density profile has a smaller effective value but the total temperature is a little bit higher. The left peak in the temperature profile is also a little bit narrower than in the observational data while the right peak is a little bit higher than the observed one. The perturbation in B_y is a little bit smaller than in the case of absence of charge exchange, (cf. Fig. 18 (solid line) and Fig. 17).

In case of higher total ion production rate, $Q_{\text{ion}} = 2.57 \times 10^{27}\,\text{s}^{-1}$ (Fig. 18, (dotted line)) the density profile has a higher effective value but the total temperature is a little bit lower. We can see that the density profile has a depletion on the left side and the width of the peak is smaller than in the case with no charge exchange, (cf. Fig. 18, (dotted line) and Fig. 17). The left peak in the temperature profile is also a little bit narrower than in the observational data while the right peak is a little bit higher than the observed one. The perturbation in B_y is a little bit smaller than in case of absence of charge exchange (cf. Fig. 18, (dotted line) and Fig. 17).

In a case with a higher charge exchange rate that corresponds to the maximum value of the density of atmosphere, $n_{\mathrm{atmos}} = 5 \times 10^8\,\mathrm{cm}^{-3}$ and a total ion production rate, $Q_{\mathrm{ion}} = 2.1 \times 10^{27}\,\mathrm{s}^{-1}$ we have a satisfactory agreement in the total density profile, a smaller total temperature and no agreement in the magnetic field component B_y.

Let us consider the cases with a high charge exchange rate that corresponds to the maximum value of the density of atmosphere, $n_{\mathrm{atmos}} = 10^9\,\mathrm{cm}^{-3}$ and an ionization rate of $Q_{\mathrm{ion}} = (1.4 - 2.1) \times 10^{27}\,\mathrm{s}^{-1}$. In case of low ionization rate, $Q_{\mathrm{ion}} = 1.4 \times 10^{27}\,\mathrm{s}^{-1}$, the density peak is higher and thinner than the observed one whereas the temperature profile is in a good agreement with the observation. The magnetic field B_y profile is only in qualitative agreement with observation. In the case of a higher ionization rate, $Q_{\mathrm{ion}} = 2.1 \times 10^{27}\,\mathrm{s}^{-1}$, the density has a strong double peak structure but the temperature profile is in agreement with the observations. However, the magnetic field profile has no agreement with observational data.

In previous cases we assumed that the charge exchange process is only due to the lower altitude, exponential part of the neutral atmosphere. Let us consider now the results of simulation that includes also the charge exchange due to the extended atmosphere which is distributed as r^{-2}. Figure 19 shows the profiles of the total density, temperature and magnetic field for different maximum values of the density of atmosphere, $n_{\mathrm{atmos}} = (5 \times 10^7 - 10^9)\,\mathrm{cm}^{-3}$, and an ionization rate, $Q_{\mathrm{ion}} = (3.03 - 4.04) \times 10^{27}\,\mathrm{s}^{-1}$.

Let us consider first the cases with a low maximum value of the density of atmosphere, $n_{\mathrm{atmos}} = 5 \times 10^7\,\mathrm{cm}^{-3}$, and an ionization rate of $Q_{\mathrm{ion}} = (3.03 - 4.04) \times 10^{27}\,\mathrm{s}^{-1}$. In case of lower ionization rate, $Q_{\mathrm{ion}} = 3.03 \times 10^{27}\,\mathrm{s}^{-3}$, the density profile is in agreement with the observation, but the temperature is a little bit higher in the peaks (Fig. 19, solid line). The magnetic field profile (B_y) is in a qualitative agreement with the observation (Fig. 19, solid line). In the case of higher ionization rate, $Q_{\text{ion}} = 4.04 \times 10^{27}\,\text{s}^{-1}$, the density profile is a little bit higher in peak than the observed one and the temperature is a little bit lower in the left peak. The magnetic field profile (B_y) is much smoother than in the observation (not shown in Fig. 19).

In the cases with a higher maximum atmosphere density, $n_{\text{atmos}} = 10^8\,\text{cm}^{-3}$, the maximum value of the wake density becomes much higher than in the observation. Although the temperature profiles are in good agreement with the observations, the magnetic field component B_y is much smoother in the case of $Q_{\text{ion}} = 3.03 \times 10^{27}\,\text{s}^{-1}$ (Fig. 19, (dotted line)), and it is in qualitative agreement with the observations in the case with $Q_{\text{ion}} = 4.04 \times 10^{27}\,\text{s}^{-1}$ (not shown in Fig. 19). The increase in the atmosphere maximum to $n_{\text{atmos}} = 5 \times 10^8\,\text{s}^{-3}$ results in an increase of the density to more than twice the observed value. In this case we have $Q_{\text{ion}} = 4.04 \times 10^{27}\,\text{s}^{-1}$ with a total charge exchange rate of $Q_{\text{exch}} = 5.8 \times 10^{28}\,\text{s}^{-1}$, Fig. 19, (dashed line).

In case of a high maximum atmosphere density, $n_{\text{atmos}} = 10^9\,\text{cm}^{-3}$ there is no similarity between simulation and observation. We simulated the cases with ionization rates, $Q_{\text{ion}} = (2.1 - 4.04) \times 10^{27}\,\text{s}^{-1}$. In the case of low ionization rate, $Q_{\text{ion}} = 2.1 \times 10^{27}\,\text{s}^{-1}$, the density profile has two thin peaks (Fig. 19, (dot-dashed line)) while the magnetic field profile (B_y) has a strong variation (Fig. 19, (dot-dashed line)) that does not correspond the observation. In case of moderate ionization rate, $Q_{\text{ion}} = 3.03 \times 10^{27}\,\text{s}^{-1}$, the density profile has one peak with a value, $n_{\text{total}} > 10 n_0$

that is much higher than observed one whereas the magnetic field profile (B_y) is much smoother than observed one. In the case of a high ionization rate, $Q_{\text{ion}} = 4.2 \times 10^{27}\,\text{s}^{-1}$, the density profile has one peak with a value, $n_{\text{total}} \approx (8 - 10)n_0$ that is much higher than observed whereas the magnetic field profile (B_y) is much smoother than observed.

One of the main issues of the plasma torus – Io interaction is the question about the real obstacle in this interaction. There are two possible candidates for this problem - (1) mass loading by the pickup ions originally produced from Io's atmosphere by the ionization processes or charge exchange processes between the incoming plasma torus ions and the neutral atmosphere, or (2) charge exchange processes between the pickup ions originally produced from Io's atmosphere and the neutral atmosphere. **Table 1 gives a summary of results of simulations for different models that are considered in this section.**

In the case of the models with a high density of Io's atmosphere $(10^9\,\text{cm}^{-3})$ the charge exchange rate becomes very high, $Q_{\text{exch}} \approx (6.7 - 9) \times 10^{28}\,\text{s}^{-1}$ **(cases ceie6, ceie7 and seie8, Table 1)**. Note that in these cases the charge exchange rate for incoming ions is much smaller than for pickup ions. We compared the charge exchange rate in the external $(r > 4H_{\text{atmos}})$ and the internal $(r \leq 4 \times H_{\text{atmos}})$ region. The charge exchange rate for incoming ions in the external region has approximately the same value as a charge exchange rate in the internal region. However, the charge exchange rate for pickup ions in the external region is approximately 20 times smaller than the charge exchange rate in the internal region.

The magnetic field profile (B_y) does not match the observational data very well for a small ionization rate, $Q_{\mathrm{ion}} = 2.1 \times 10^{27}\mathrm{s}^{-1}$ **(case ceie3, Table 1)**, whereas the total density value in the plasma wake is much more than observed one in the case of higher ionization rate, $Q_{\mathrm{ion}} = (3.03 - 4.04) \times 10^{27}\mathrm{s}^{-1}$ **(cases ceiel and ceie2, Table 1)**. Hence, the models with a high charge exchange rate, $Q_{\mathrm{exch}} = (6.5 - 9) \times 10^{28}\,\mathrm{s}^{-1}$, are not realistic because they cannot explain the observational data.

The model with $n_{\mathrm{atmos}} = 5 \times 10^{8}\,\mathrm{cm}^{-3}$ **(case ceie5, Table 1)**, gives the total charge exchange rate $Q_{\mathrm{exch}} = 5.8 \times 10^{28}\,\mathrm{s}^{-1}$. The models with $n_{\mathrm{atmos}} = 10^{8}\,\mathrm{cm}^{-3}$ **(cases ceie3 and ceie4, Table 1)**, give total charge exchange rates of $Q_{\mathrm{exch}} = (1.09 - 1.35) \times 10^{28}\,\mathrm{s}^{-1}$ And, finally, the models with $n_{\mathrm{atmos}} = 5 \times 10^{7}\,\mathrm{cm}^{-3}$, give total charge exchange rates of $Q_{\mathrm{exch}} = (6.12 - 6.54) \times 10^{27}\,\mathrm{s}^{-1}$ **(cases ceiel and ceie2, Table 1).**

The analysis of the models shows that two cases that have a good fit for observational data. In the model without charge exchange **(case nce, Table 1)** the simulation results describe well enough the main observational data - a total density, a total temperature and the magnetic field (B_y) (Fig. 17). The more realistic model with $n_{\mathrm{atmos}} = 5 \times 10^{7}\,\mathrm{cm}^{-3}$, and ionization rate $Q_{\mathrm{ion}} = 3.03 \times 10^{27}\,\mathrm{s}^{-1}$ **(case ceiel, Table 1)**, also fits satisfactorily the observational data (Fig. 19, solid line). This model gives the charge exchange rates $Q_{\mathrm{p,exch}} = 3.16 \times 10^{27}\,\mathrm{s}^{-1}$ and $Q_{\mathrm{c,exch}} = 3.13 \times 10^{27}\,\mathrm{s}^{-1}$ for plasma torus ions and pickup ions respectively and would correspond to an MHD model with total fresh ion mass-loading rate and the charge exchange rate, which contributes to the momentum and energy friction terms, of $1.2 \times 10^{28}\,\mathrm{s}^{-1}$ (Combi, Gombosi and Kabin, 2002). So, we find that the interaction is dominated in roughly equal parts between primary torus ion charge exchange and secondary pickup ion charge exchange.

4. Conclusions

3D Boltzmann simulations of the interaction of the Jovian plasma torus with Io, have demonstrated several new features:

- The whistler (lead front) and quasi-stationary Alfvén waves (wings) strongly affect plasma flow around Io.
- The effect of the finite ion gyroradius that results in formation of the asymmetrical boundary layer in the vicinity of Io's ionosphere is important. The plasma parameters have a strongly asymmetrical distribution across Io's wake. The kinetic behavior of ion dynamics reproduces the inverse structure of the magnetic field (due to drift current) which cannot be explained by standard MHD or electrodynamic simulations which do not account for anisotropic ion pressure. The diamagnetic effect of non-isotropic gyrating pickup ions broadens the B-field perturbation and produces increased temperatures in the flanks of the wake, as observed by the Galileo spacecraft, but not explained by previous simulations. **Note that two-fluid simulation (Saur et al., 2002) produces the double-peak signature with spatial scale much smaller than in observation.**
- The cold, dense wake is produced, as in MHD, but was not produced in electromagnetic simulations without ad hoc addition of bidirectional electrons.
- The values of temperatures of the electrons which are created and cooled by

collision with neutrals in the exosphere and inside the ionosphere may strongly affect the pickup ion dynamics along the magnetic field and consequently the pick up distribution across the wake. In the absence of an observed global picture of the plasma distribution, the simulation serves to demonstrate the wide range of global configurations that are possible for various electron temperature descriptions. A full hybrid simulation for the plasma including an electron temperature treatment that accounts for electron-neutral collision and a detailed neutral description would be required to produce an accurate global picture from the first principles.

- The effective conductivity of Io's ionosphere may change strongly the distribution of the magnetic field near and inside Io. The reduced conductivity ($l_{dif} = 0.025$) near the ionosphere and inside the Io may reduce the magnetic field inside Io by $20 - 40\%$ and the peak of the plasma density at the Galileo trajectory by 15%.
- The best models that fit the observational data well are: the model without charge exchange and ionization rate $Q_{\text{ion}} = 4.8 \times 10^{27}\,\text{s}^{-1}$, and the model with ionization rate $Q_{\text{ion}} = 3.03 \times 10^{27}\,\text{s}^{-1}$ and the total charge exchange rate $Q_{\text{exch}} = 6.3 \times 10^{27}\,\text{s}^{-1}$. The best MHD model had a total fresh ion mass-loading rate of $6 \times 10^{27}\,\text{s}^{-1}$ and a charge exchange rate, which contributes to the momentum and energy friction terms, of $1.2 \times 10^{28}\,\text{s}^{-1}$ (Combi, Gombosi and Kabin, 2002). The reason for the factor of 2 difference results from the above-described pressure anisotropy effect in the kinetic simulation, and the resulting tighter plasma distribution near the equator plane defined by Io.

- **In the presented calculations the value of the ion gyroradius was much larger than the realistic value. So we have to investigate the effects of realistic values of the ion gyroradius in future simulations. We expect that the smaller ion gyroradius may result in smaller asymmetry of the global picture. However, we do not expect the strong changes in the plasma and the magnetic field profiles because the used value of the ion gyroradius is much smaller than the characteristic scale of the problem - the radius of Io. These profiles are controlled primary by the inter-penetration of the torus plasma and the pickup ions.**

Acknowledgments. A.S.L. and M.R.C. were supported in part by the NASA Grant NAG5-9464 from the Applied Information Systems Research Program and NAG5-12822 from The Planetary Atmospheres Program. Computational resources were provided by the San Diego Super Computer Center (IBM Blue-Horizon), the Center for Advanced Computing Univ. of Michigan (IBM POWER 3 Cluster), the National Partnership for Advanced Computational Infrastructure, and the Computer Center TU of Braunschweig (Alpha-Cluster). The authors thank Andreas Kopp and other referee for their helpful comments. A.S.L thanks D. Markiewicz-Innes for her helpful comments.

References

Braginskii, S.L., Transport processes in a plasma. In: Leontovich, M.A. (Ed.), Reviews of Plasma Physics. Consultants Bureau, New York, pp. 205-240.

Cloutier, P.A., Daniell, R.E., Dessler, A.J., and Hill, T.W., 1978. A cometary ionosphere model for Io. Astrophys. Space Sci. 55, 93-112.

Combi, M.R., Gombosi, T.I. and Kabin, K., 2002. Plasma Flow Past Cometary and Planetary Satellite Atmospheres. In: Mendillo, M., Nagy, A., Waite, J.H. (Eds.), Atmospheres in the Solar System: Comparative Aeronomy. Geophys. Monograph Series Vol. 130. AGU Washington, D.C., pp. 151-167.

Combi, M.R., Kabin, K., Gombosi, T., De Zeeuw, D.L., and Powell, K., 1998. Io's plasma environment during the Galileo flyby: Global three-dimensional MHD modeling with adaptive mesh refinement. J. Geophys. Res. 103, 9071-9081.

Frank, L.A., Paterson, W.R., Ackerson, K.L., Vasyliunas, V.M., Coroniti, F.V., and Bolton, S.J., 1996. Plasma observations at Io with the Galileo spacecraft. Science, 274, 394-395.

Frank, L.A., and Paterson, W.R., 2000. Return to Io by the Galileo spacecraft: Plasma observation. J. Geophys. Res. 105, 25363-25378.

Gurnett, D.A., Kurth, W.S., Roux, A., Bolton, S.J., Kennel, C.F., 1996. Galileo Plasma Wave Observations in the Io Plasma Torus and Near Io. Science. 274, 391-392.

Goertz, C.K., 1980. Io's interaction with the plasma torus. J. Geophys. Res. 85, 2949-2956.

Ip, W.-H., 1990. Neutral gas-plasma interaction: The case of the Io plasma torus. Adv. Space Res. 10(1), 15-18.

Kabin, K., Combi, M.R., Gombosi, T.I., DeZeeuw, D.L., Hansen, K.S., and Powell, K.G., 2001. Io's magnetospheric interaction: an MHD model with day-night asymmetry. Planetary and Space Sci. 49, 337-344.

Kivelson, M.G., Khurana, K.K., Walker, R.J., Warnecke, J., Russell, C.T., Linker, J.A., Southwood, D.J., and Polanskey, C., 1996. Io's interaction with the plasma torus: Galileo magnetometer report. Science 274, 396-398.

Kivelson, M.G., Khurana, K.K., Russell, C.T., Joy, S.P., Volwerk, M., Walker, R.J., Zimmer, Ch., and Linker, J.A., 2001. Magnetized or unmagnetized: Ambiguity persists following Galileo's encounters with Io in 1999 and 2000. J. Geophys. Res. 106, 26121-26136.

Kopp, A., 1996. Modifications of the electrodynamic interaction between Jupiter and Io due to mass loading effects. J. Geophys. Res. 101, 24943-24954.

Kopp, A., Birk, G.T., Otto, A., 1998. On the formation of Io-induced acceleration region related to Jovian aurora. Planet. Space Sci. 46, 405-415.

Lellouch, E., 1996. Urey Prize Lecture. Io's Atmosphere: not yet understood. Icarus 124, 1-21.

Linker, J.A., Khurana, K.K., Kivelson, M.G., and Walker, R.J., 1991. A three-dimensional MHD simulation of plasma flow past Io. J. Geophys. Res. 96, 21037-21053.

Linker, J.A., Khurana, K.K., Kivelson, M.G., and Walker, R.J., 1998. MHD simulation of Io's interaction with the plasma torus. J. Geophys. Res. 103(E9), 19867-19877.

Linker, J.A., Kivelson, M.G., and Walker, R.J., 1989. The effect of mass loading on the temperature of a flowing plasma. Geophys. Res. Lett. 16(7), 763-766.

Lipatov, A. S., 2002. The Hybrid Multiscale Simulation Technology. An introduction with application to astrophysical and laboratory plasmas. Springer-Verlag, Berlin, Heidelberg and New York.

Lipatov A.S., Zank, G.P., Pauls, H.L., 1998. The Dynamics of an *H* Neutral Component inside the Heliosphere: 2.5D Particle-Mesh Boltzmann Simulation. J. Geophys. Res. 103, 20636, 1998.

Malama, Y.G., 1991. Monte-Carlo simulation of neutral atoms trajectories in the solar system. Astrophys. Space Sci. 176, 21-39.

Neubauer, F.M., 1980. Nonlinear standing Alfvén wave current system at Io - Theory. J. Geophys. Res. 85, 1171-1178.

Ripkin, H.L., Fahr, H.J., 1983. Modification of the local interstellar gas properties in the heliospheric interface. Astron. astrophys. 122, 181-190.

Saur, J., Neubauer, F.M., Strobel, D.F., and Summers, M.E., 1999. Three-dimensional plasma simulation of Io's interaction with the Io plasma torus: Asymmetric plasma flow. J. Geophys. Res. 104, 25105.

Saur, J., Neubauer, F.M., Strobel, D.F., and Summers, M.E., 2002. Interpretation of Galileo's Io plasma and field observations: I0, I24, and I27 flybys and close polar passes. J. Geophys. Res. 107, 1422.

Saur, J., Strobel, D.F., Neubauer, F.M., and Summers, M.E., 2003. The ion mass loading rate at Io. Icarus 163(2), 456-468.

Southwood, D.J., and Dunlop, M.W., 1984. Mass pickup in sub-Alfvénic plasma flow: A case study for Io. Planet. Space Sci. 32, 1079-1089.

Southwood, D.J., Kivelson, M.G., Walker, R.J., and Slavin, J.A., 1980. Io and its plasma environment. J. Geophys. Res. 85, 5959-5968.

Umeda, T., Omura, Y., Matsumoto, H., 2001. An improved masking method for absorbing boundaries in electromagnetic particle simulations, Comp. Phys. Comm. (137), 286-299.

Van'yan, L.L. and Lipatov, A.S., 1972. Three-dimensional hydromagnetic disturbances generated by a magnetic dipole in an anisotropic plasma. Geomagn. and Aeronomy 18(5), 316-318.

Williams, D.J., et al., 1996. Electron beams and ion composition measured at Io and its torus. Science. 274, 401-403.

Williams, D.J., Thorne, R.M., and Mauk, B., 1999. Energetic electron beams and trapped electrons at Io. J. Geophys. Res. 104, 14739-14753.

Wolf-Gladrow, D.A., Neubauer, F.M., and Lussem, M., 1987. Io's interaction with the plasma torus: A self-consistent model. J. Geophys. Res. 92, 9949-9961.

Zueva, N.M., Imshennik, V.S., Lokutsievskii, O.B., Mikhailov, M.S., 1975. The model of nonhydrodynamical stage of plasma focus. Preprint No. 73. Keldysh Institute of Applied Mathematics, Moscow.

A. S. Lipatov and M. R. Combi, Space Physics Research Laboratory, Department of Atmospheric, Oceanic and Space Sciences, The University of Michigan, Ann Arbor, MI 48109-2143, USA, (emails: alipatov@engin.umich.edu, mcombi@umich.edu)

Received ____________________

To appear in the *ICARUS*, 2004

5. Figure captions

Figure 1. Galileo trajectory close to Io and the system of coordinates.

Figure 2. Incoming (top) and pickup (bottom) ion density in the x-z plane. The case with $Q_{\rm ion} = 3.03 \times 10^{27}\,{\rm s}^{-1}$, $n_{atmos} = 5 \times 10^{7}\,{\rm cm}^{-3}$, $\beta_{e,PI} = \beta_e$, $\beta_{e,iono} = 0.25\beta_e$, $W_{ext} = 5\%$, and $H_{atmos} = 0.06$. See explanation in Fig. 6.

Figure 3. Incoming (top) and pickup (bottom) ion density in the y-z plane for the same parameters as Fig. 2. See explanation in Fig. 7.

Figure 4. Electric (top) and magnetic (bottom) fields in the x-z plane for the same parameters as Fig. 2. Figure shows a strong asymmetry of the electromagnetic field due to finite gyroradius effects.

Figure 5. Electric (top) and magnetic (bottom) fields in the y-z plane for the same parameters as Fig. 2. Figure shows the formation of an Alfvén wing in the direction of the main magnetic field.

Figure 6. Incoming (top) and pickup (bottom) ion velocity arrows in the x-z plane for the same parameters as Fig. 2. The figure demonstrates a flow of pickup ions from the "corona" across the magnetic field. The incoming ions flow around the effective obstacle that is produced by pickup ions and ionosphere.

Figure 7. Incoming (top) and pickup (bottom) ion velocity arrows in the y-z plane for the same parameters as Fig. 2. The figure demonstrates a strong expansion of pickup ion "corona" along the magnetic field line. The incoming ions flow around the region of extended "corona".

Figure 8. Two-dimensional section for total density in the x-y plane for the same parameters as Fig. 2.

Figure 9. Total density, temperature and magnetic field along the x-axis. The case with $\beta_{e,PI} = 0$, $\beta_{e,iono} = 0$, $W_{ext} = 0\%$, and $H_{atmos} = 0.06$.

Figure 10. Two-dimensional section for total density in the x-y plane. The case with $\beta_{e,PI} = 0$, $\beta_{e,iono} = 0$, $W_{ext} = 0\%$, and $H_{atmos} = 0.06$.

Figure 11. Total density, temperature and magnetic field along the x-axis. The case with $\beta_{e,PI} = \beta_e$, $\beta_{e,iono} = 0$, $W_{ext} = 0\%$, and $H_{atmos} = 0.06$.

Figure 12. Two-dimensional section for total density in the x-y plane. The case with $\beta_{e,PI} = \beta_e$, $\beta_{e,iono} = 0$, $W_{ext} = 0\%$, and $H_{atmos} = 0.06$.

Figure 13. Total density, temperature and magnetic field along the x-axis. The case with $\beta_{e,PI} = \beta_e$, $\beta_{e,iono} = \beta_e$, $W_{ext} = 0\%$, $H_{atmos} = 0.06$.

Figure 14. Two-dimensional section for total density in the x-y plane. The case with $\beta_{e,PI} = \beta_e$, $\beta_{e,iono} = \beta_e$, $W_{ext} = 0\%$, $H_{atmos} = 0.06$.

Figure 15. Two-dimensional sections for pickup ion density in the x-y plane. The cases with (top) $\beta_{e,PI} = 0$, $\beta_{e,iono} = 0$; (middle) $\beta_{e,PI} = \beta_e$, $\beta_{e,iono} = 0$; (bottom) $\beta_{e,PI} = \beta_e$, $\beta_{e,iono} = 0.25\beta_e$. $W_{ext} = 0\%$, and $H_{atmos} = 0.06$. Figure demonstrates asymmetry of pickup ion density across the wake.

Figure 16. Total density, temperature and magnetic field along the x-axis for $\beta_{e,PI} = \beta_e$, $\beta_{e,iono} = 0.25\beta_e$, $H_{atmos} = 0.06$, $l_{d,up} = 0.0025$. (solid line) $W_{ext} = 10\%$, $l_{d,iono} = 0.0025$; (dotted line) $W_{ext} = 30\%$, $l_{d,iono} = 0.0025$; (dashed line) $W_{ext} = 10\%$, $l_{d,iono} = 0.025$.

Figure 17. Comparison of Galileo PLS (I0 pass) [*Frank et al.*, 1996] and MAG [*Kivelson et al.*, 1996] (the open circles) data with the Io hybrid model results in absence of charge exchange. $Q = 4.8 \times 10^{27}\,\mathrm{s}^{-1}$, $\beta_{e,PI} = 0.125\beta_e$, $\beta_{e,iono} = 0.125\beta_e$, $W_{ext} = 5\%$, $H_{atmos} = 0.06$, and $n_{iono} = 800(100)n_0$. $l_{d,up} = 0.00125$ and $l_{d,Io} = 0.0125$.

Figure 18. Same as Fig. 17, but with charge exchange ($B \exp \frac{r - r_{Io}}{H_{atmos}}$), $n_{atmos} = 10^8\,\mathrm{cm}^{-3}$: (solid line) $Q = 2.27 \times 10^{27}\,\mathrm{s}^{-1}$; (dashed line) $Q = 2.57 \times 10^{27}\,\mathrm{s}^{-1}$.

Figure 19. Same as Fig. 17, but with charge exchange ($\frac{A}{r^2} + B \exp \frac{r - r_{Io}}{H_{atmos}}$): (solid line) $n_{atmos} = 5 \times 10^7\,\mathrm{cm}^{-3}$, $n_{iono} = n_0$, $Q = 3.03 \times 10^{27}\,\mathrm{s}^{-1}$, $Q_{p,exch} = 3.169 \times 10^{27}\,\mathrm{s}^{-1}$, $Q_{c,exch} = 3.13 \times 10^{27}\,\mathrm{s}^{-1}$, $l_{d,Io} = 0.00125$; (dotted line) $n_{atmos} = 10^8\,\mathrm{cm}^{-3}$, $n_{iono} = n_0$, $Q = 3.03 \times 10^{27}\,\mathrm{s}^{-1}$, $Q_{p,exch} = 5.27 \times 10^{27}\,\mathrm{s}^{-1}$, $Q_{c,exch} = 5.6 \times 10^{27}\,\mathrm{s}^{-1}$, $l_{d,Io} = 0.00125$; (dashed line) $n_{atmos} = 5 \times 10^8\,\mathrm{cm}^{-3}$, $n_{iono} = n_0$, $Q = 4.04 \times 10^{27}\,\mathrm{s}^{-1}$, $Q_{p,exch} = 1.83 \times 10^{28}\,\mathrm{s}^{-1}$, $Q_{c,exch} = 3.97 \times 10^{28}\,\mathrm{s}^{-1}$, $l_{d,Io} = 0.0125$; (dot-dashed line) $n_{atmos} = 10^9\,\mathrm{cm}^{-3}$, $n_{iono} = n_0$, $Q = 2.1 \times 10^{27}\,\mathrm{s}^{-1}$, $Q_{p,exch} = 2.95 \times 10^{28}\,\mathrm{s}^{-1}$, $Q_{c,exch} = 3.75 \times 10^{28}\,\mathrm{s}^{-1}$, $l_{d,Io} = 0.0125$.

Table 1. Dependence of torus ion charge exchange rate and pickup ion charge exchange rate versus the maximum value of atmospherical density and ionization rate ($Q_0 = 10^{27}\,{\rm s}^{-1}$). * denote the regimes that fit satisfactory the observational data

case	$\frac{n_{\rm atmos}}{10^8\,{\rm cm}^{-3}}$	$\frac{Q_{\rm ion}}{Q_0}$	$\frac{Q_{\rm p,exch}}{Q_0}$	$\frac{Q_{\rm c,exch}}{Q_0}$	Comments
	model	without	charge	exchange	
nce		4.8	0	0	a density is a little bit wide and it is in good agreement with an observation, temperature and magnetic field are in a good agreement with an observation, Fig. 17*
	models	with	charge	exchange	in the internal region ($n_{\rm neutral} \approx B \exp \frac{r - r_{\rm Io}}{H_{\rm atmos}}$)
cei1	1	2.27			density, temperature and B_y in satisfactory agreement with observation, Fig. 18, (solid line)
cei2	1	2.57			density and temperature in satisfactory agreement with observation, B_y component is a weaker than observed, Fig. 18, (dashed line)
cei3	5	2.1			density in good agreement with observation; temperature and B_y are not in agreement with observation
cei4	10	1.4	12.6	14	density with strong narrow peak, temperature in satisfactory agreement with observation; B_y is weaker than observed
cei5	10	2.1	12	20.2	density with two peaks, temperature is in satisfactory agreement with observation; B_y has much stronger depletion than in observation
	models	with	charge	exchange	in the internal and external region ($n_{\rm neutral} \approx \frac{A}{r^2} + B \exp \frac{r - r_{\rm Io}}{H_{\rm atmos}}$)
ceie1	0.5	3.03	3.169	3.13	density, temperature and B_y in good agreement with observation, Fig. 19*, (solid line)
ceie2	0.5	4.04	2.67	3.87	density and temperature in satisfactory agreement with observation, B_y is a weaker than observed
ceie3	1	3.03	5.27	5.6	density is higher than the observation, variation in B_y is a weaker than observed, Fig. 19, (dotted line)
ceie4	1	4.04	5.55	7.93	density is higher than observation, variation in B_y is weaker than observed
ceie5	5	4.04	18.3	39.7	density is much higher than in an observation, variation in the B_y is strong but profile is wider than observed, Fig. 19, (dashed line)
ceie6	10	2.1	29.5	37.5	two-peak density profile, variation in the B_y is much stronger than observed, Fig. 19, (dot-dashed line)
ceie7	10	3.03	28.	44.8	density is much higher than in observation, variation in the B_y is much weaker than observed
ceie8	10	4.04	27.5	60.	density is much higher than in observation, variation in B_y is much weaker than observed

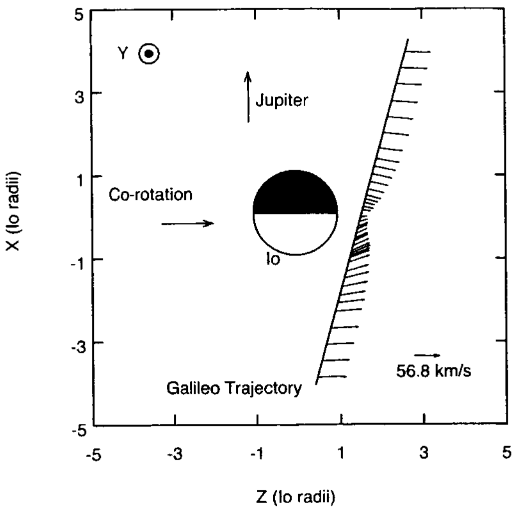

Figure 1. Galileo trajectory close to Io and the system of coordinates.

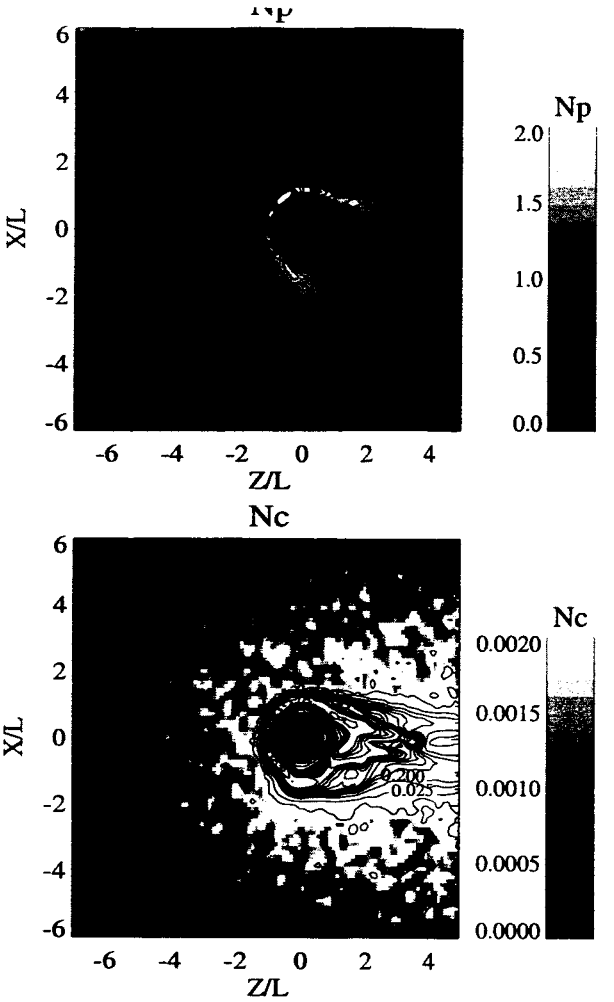

Figure 2. Incoming (top) and pickup (bottom) ion density in the x-z plane. The case ceiel (Table 1) with $\beta_{\mathrm{e,PI}} = \beta_{\mathrm{e}}$, $\beta_{\mathrm{e,iono}} = 0.25\beta_{\mathrm{e}}$, $W_{ext} = 5\%$, and $H_{\mathrm{atmos}} = 0.06$. See explanation in Fig. 6.

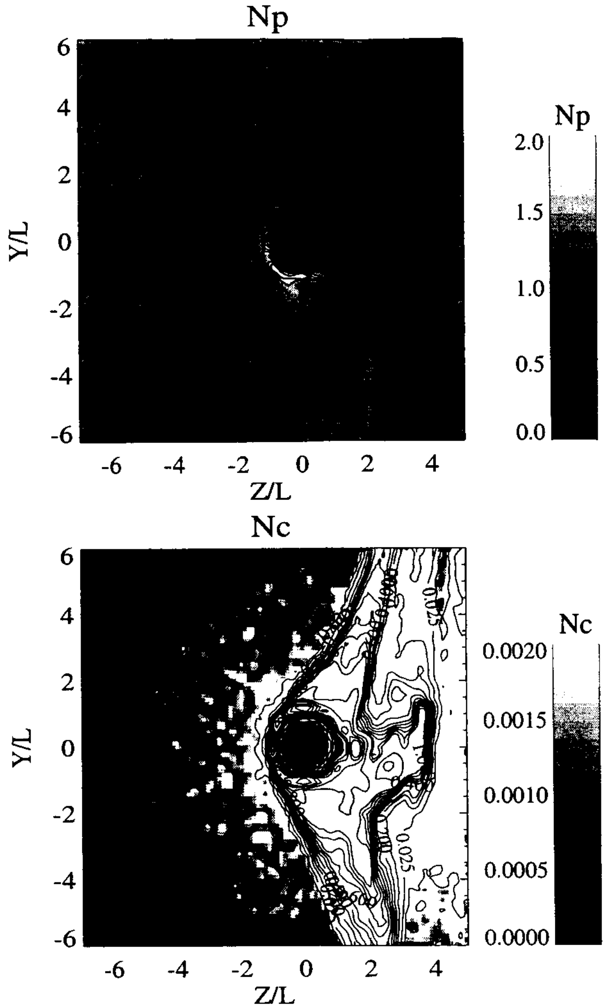

Figure 3. Incoming (top) and pickup (bottom) ion density in the y-z plane for the same parameters as in Fig. 2. See explanation in Fig. 7.

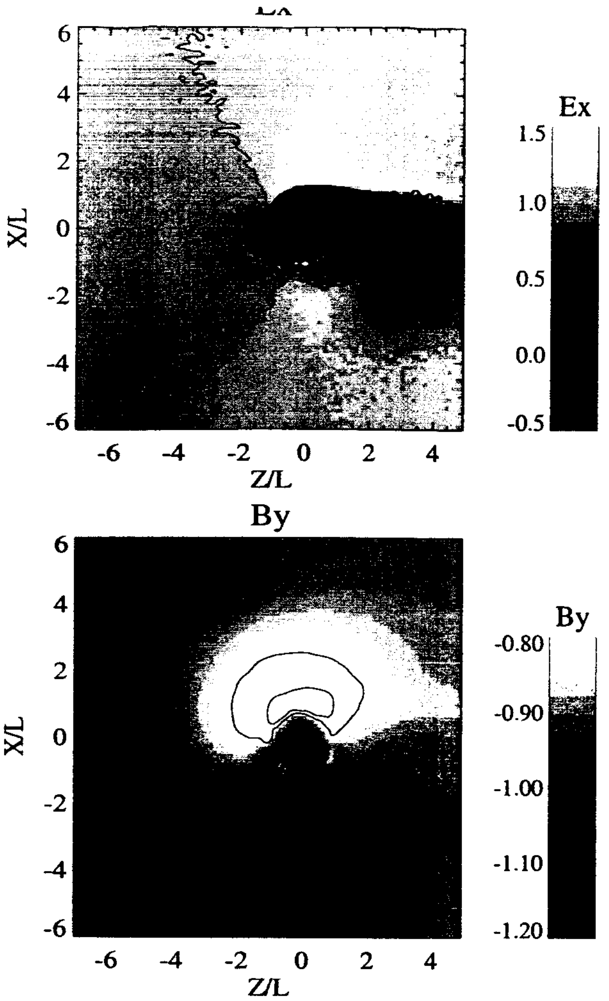

Figure 4. Electric (top) and magnetic (bottom) fields in the x-z plane for the same parameters as in Fig. 2. Figure shows a strong asymmetry of the electromagnetic field due to finite gyroradius effects.

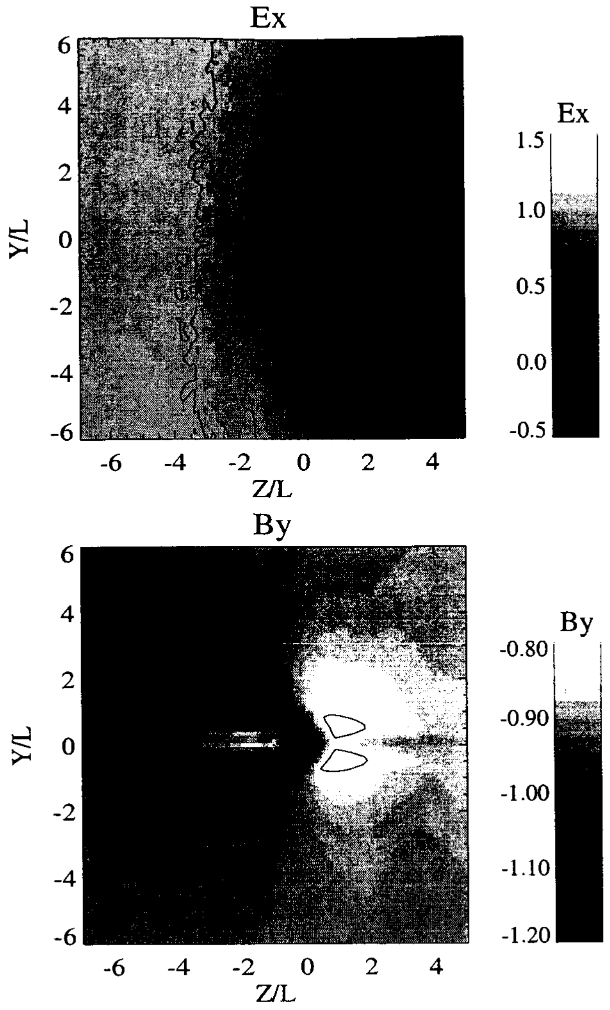

Figure 5. Electric (top) and magnetic (bottom) fields in the y-z plane for the same parameters as in Fig. 2. Figure shows the formation of an Alfvén wing in the direction of the main magnetic field.

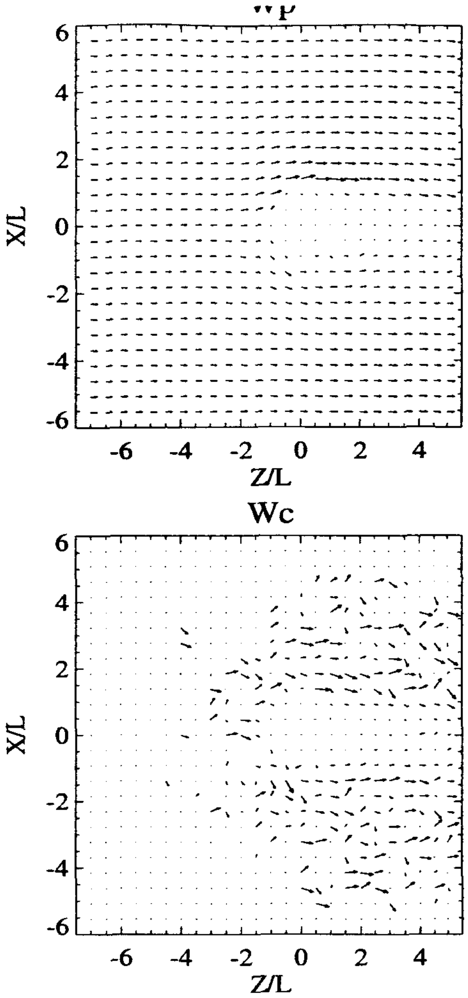

Figure 6. Incoming (top) and pickup (bottom) ion velocity arrows in the x-z plane for the same parameters as in Fig. 2. The figure demonstrates a flow of pickup ions from the "corona" across the magnetic field. The incoming ions flow around the effective obstacle that is produced by pickup ions and ionosphere.

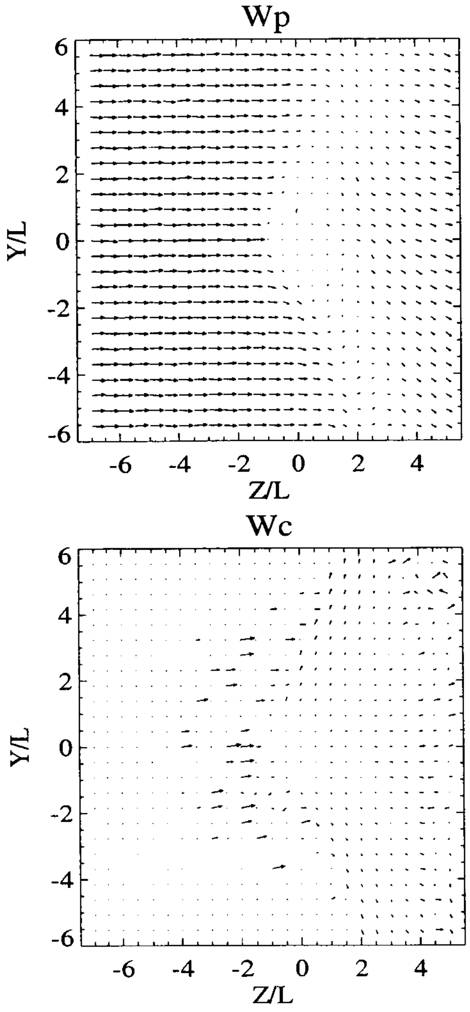

Figure 7. Incoming (top) and pickup (bottom) ion velocity arrows in the y-z plane for the same parameters as in Fig. 2. The figure demonstrates a strong expansion of pickup ion "corona" along the magnetic field line. The incoming ions flow around the region of extended "corona".

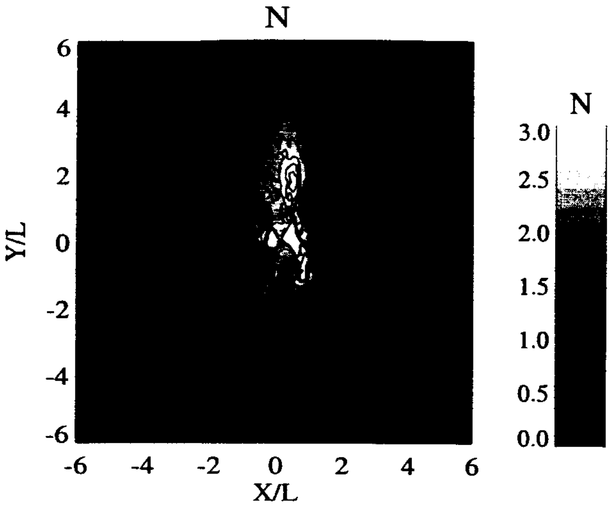

Figure 8. Two-dimensional cross section for total density in the x-y plane at $z = 1.5r_{\mathrm{Io}}$ for the same parameters as in Fig. 2.

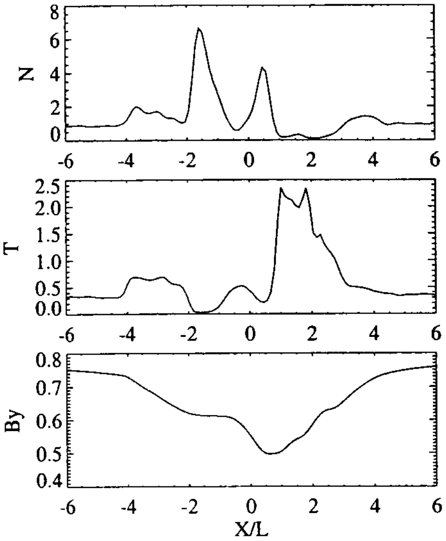

Figure 9. Total density, temperature and magnetic field along the x-axis at $z = 1.5r_{\mathrm{Io}}$. The case with $\beta_{\mathrm{e,PI}} = 0$, $\beta_{\mathrm{e,iono}} = 0$, $W_{ext} = 0\%$, and $H_{\mathrm{atmos}} = 0.06$.

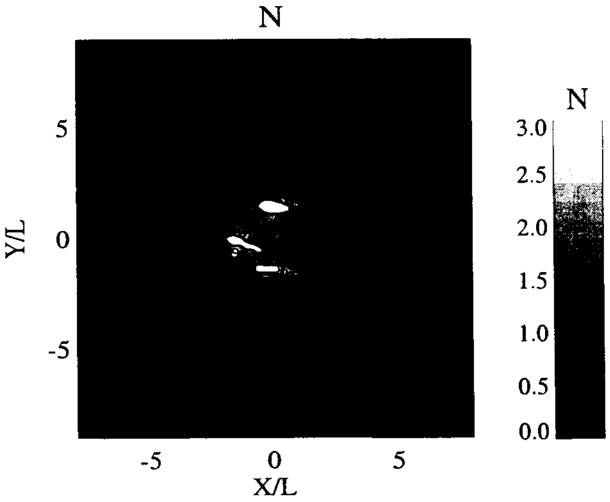

Figure 10. Two-dimensional cross section for total density in the x-y plane at $z = 1.5r_{\mathrm{Io}}$. The case with $\beta_{\mathrm{e,PI}} = 0$, $\beta_{\mathrm{e,iono}} = 0$, $W_{ext} = 0\%$, and $H_{\mathrm{atmos}} = 0.06$.

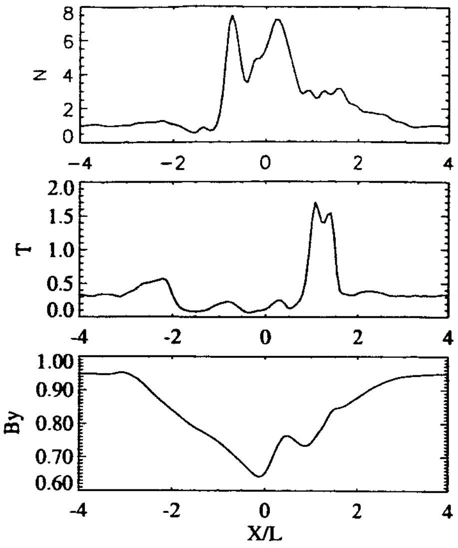

Figure 11. Total density, temperature and magnetic field along the x-axis at $z = 1.5r_{\rm Io}$. The case with $\beta_{\rm e,PI} = \beta_{\rm e}$, $\beta_{\rm e,iono} = 0$, $W_{ext} = 0\%$, and $H_{\rm atmos} = 0.06$.

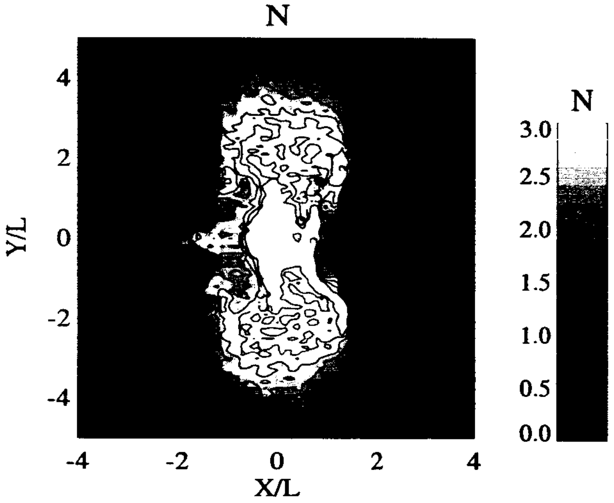

Figure 12. Two-dimensional cross section for total density in the x-y plane at $z = 1.5r_{\rm Io}$. The case with $\beta_{\rm e,PI} = \beta_{\rm e}$, $\beta_{\rm e,iono} = 0$, $W_{ext} = 0\%$, and $H_{\rm atmos} = 0.06$.

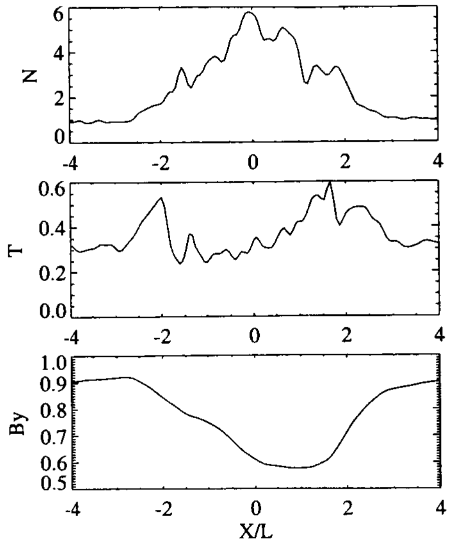

Figure 13. Total density, temperature and magnetic field along the x-axis at $z = 1.5 r_{\mathrm{Io}}$. The case with $\beta_{\mathrm{e,PI}} = \beta_{\mathrm{e}}$, $\beta_{\mathrm{e,iono}} = \beta_{\mathrm{e}}$, $W_{ext} = 0\%$, $H_{\mathrm{atmos}} = 0.06$.

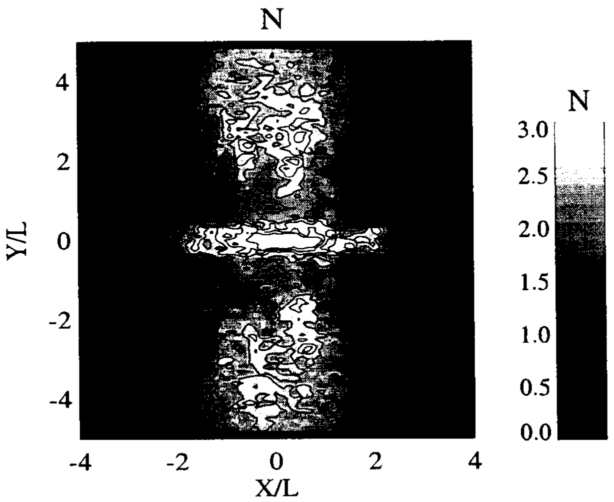

Figure 14. Two-dimensional cross section for total density in the x-y plane at $z = 1.5 r_{\mathrm{Io}}$. The case with $\beta_{\mathrm{e,PI}} = \beta_{e}$, $\beta_{\mathrm{e,iono}} = \beta_{\mathrm{e}}$, $W_{ext} = 0\%$, $H_{\mathrm{atmos}} = 0.06$.

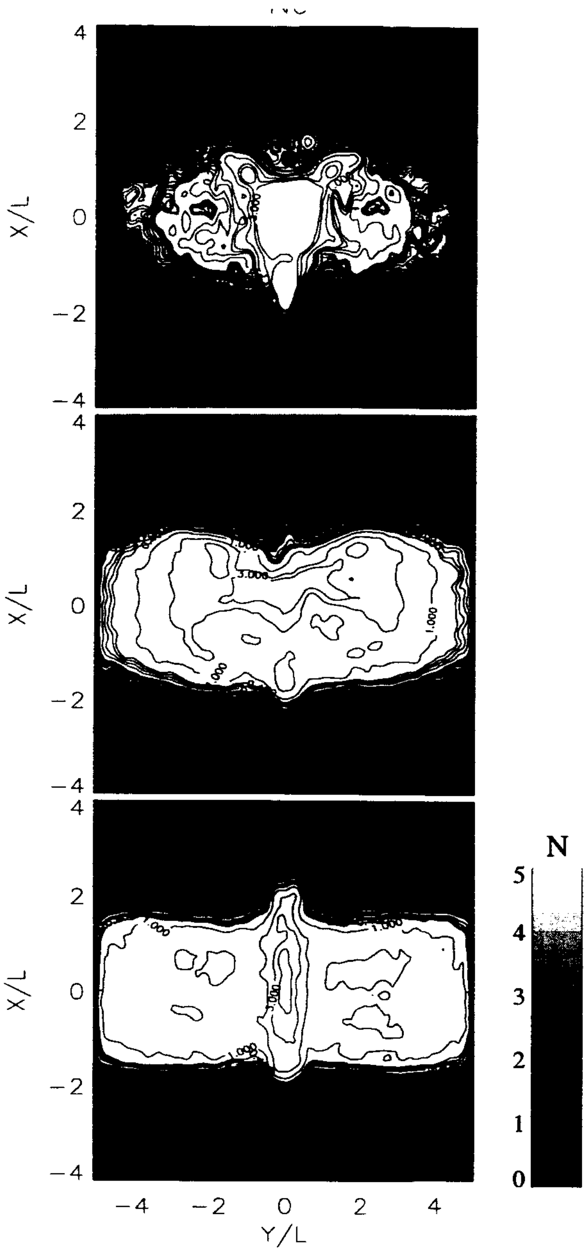

Figure 15. Two-dimensional cross sections for pickup ion density in the x-y plane at $z = 1.5r_{\rm Io}$. The cases with (top) $\beta_{\rm e,PI} = 0$, $\beta_{\rm e,iono} = 0$; (middle) $\beta_{\rm e,PI} = \beta_{\rm e}$, $\beta_{\rm e,iono} = 0$; (bottom) $\beta_{\rm e,PI} = \beta_e$, $\beta_{\rm e,iono} = 0.25\beta_e$. $W_{ext} = 0\%$, and $H_{\rm atmos} = 0.06$. Figure demonstrates asymmetry of pickup ion density across the wake.

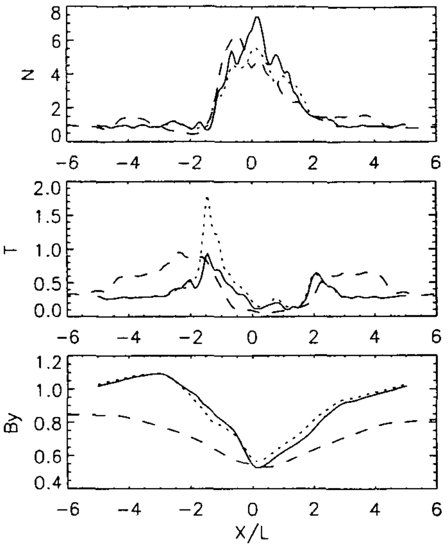

Figure 16. Total density, temperature and magnetic field along the x-axis at $z = 1.5r_{\mathrm{Io}}$ for cases with $\beta_{\mathrm{e,PI}} = \beta_{\mathrm{e}}$, $\beta_{\mathrm{e,iono}} = 0.25\beta_{\mathrm{e}}$, $H_{\mathrm{atmos}} = 0.06$, $l_{\mathrm{d,up}} = 0.0025$. (solid line) $W_{ext} = 10\%$, $l_{\mathrm{d,iono}} = 0.0025$; (dotted line) $W_{ext} = 30\%$, $l_{\mathrm{d,iono}} = 0.0025$; (dashed line) $W_{ext} = 10\%$, $l_{\mathrm{d,iono}} = 0.025$.

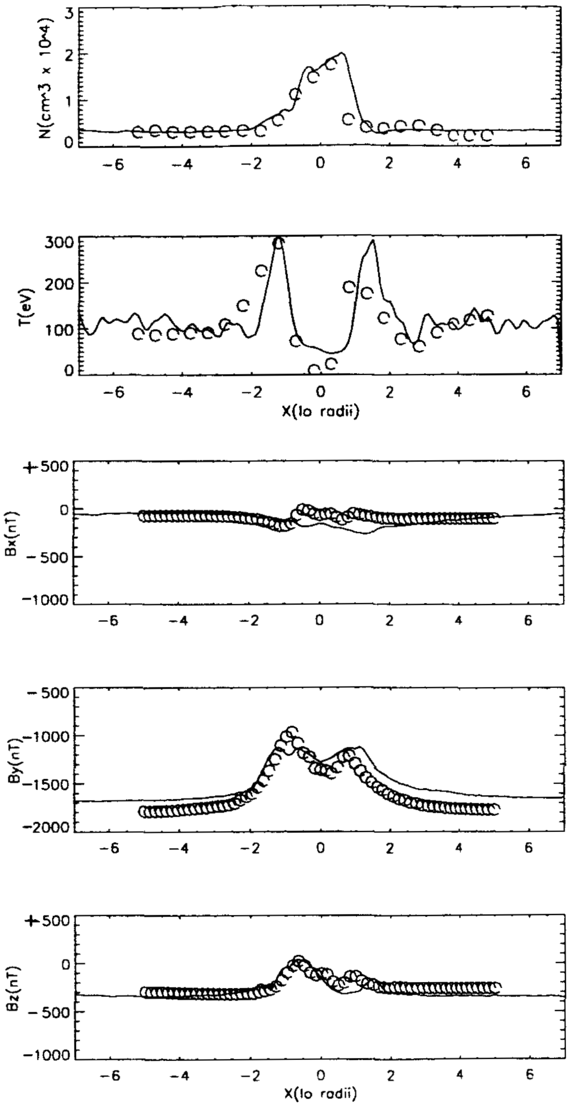

Figure 17. Comparison of Galileo PLS (I0 pass) [*Frank et al.*, 1996] and MAG [*Kivelson et al.*, 1996] (the open circles) data with the Io hybrid model results **along the trajectory** in the absence of charge exchange (case nce, Table 1). $\beta_{\mathrm{e,PI}} = 0.125\beta_{\mathrm{e}}$, $\beta_{\mathrm{e,iono}} = 0.125\beta_{\mathrm{e}}$, $W_{ext} = 5\%$, $H_{\mathrm{atmos}} = 0.06$, and $n_{\mathrm{iono}} = 800(100)n_0$. $l_{\mathrm{d,up}} = 0.00125$ and $l_{\mathrm{d,Io}} = 0.0125$.

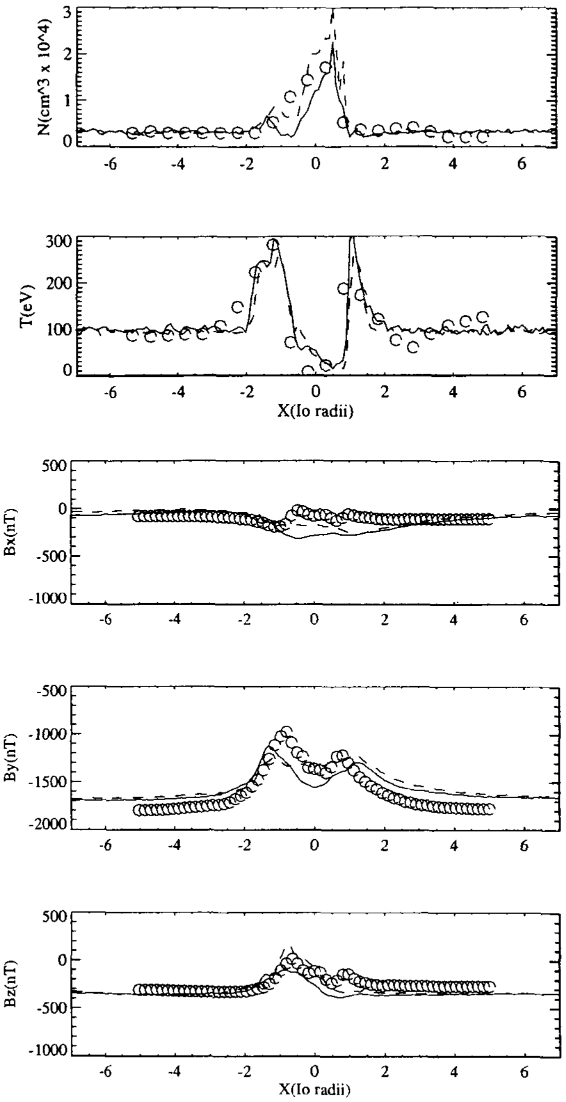

Figure 18. Same as Fig. 17, but with charge exchange ($B\exp\frac{r-r_{\mathrm{Io}}}{H_{\mathrm{atmos}}}$), $n_{\mathrm{atmos}} = 10^8\,\mathrm{cm}^{-3}$: (solid line, case ceil, Table 1); (dashed line, case cei2, Table 1).

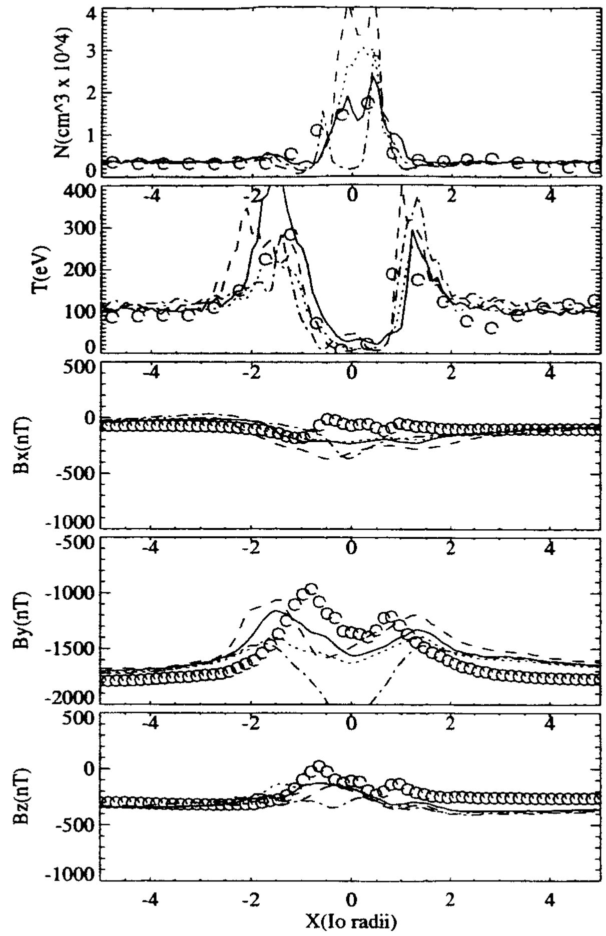

Figure 19. Same as Fig. 17, but with charge exchange ($\frac{A}{r^2}+B\exp\frac{r-r_{\rm Io}}{H_{\rm atmos}}$): (solid line, case ceie1, Table 1) $n_{\rm iono}=n_0$, $l_{\rm d,Io}=0.00125$; (dotted line, case ceie3, Table 1) $l_{\rm d,Io}=0.00125$; (dashed line, case ceie5, Table 1) $l_{\rm d,Io}=0.0125$; (dot-dashed line, case ceie6, Table 1) $l_{\rm d,Io}=0.0125$.